A Coupled Ground Heat Flux-Surface Energy Balance Model of Evaporation Using Thermal Remote Sensing Observations

Devansh Desai[1,10,11*], Kaniska Mallick[2,3*], Bimal K. Bhattacharya[1,#], Ganapati S. Bhat[4], Ross Morrison[5], Jamie Clevery[6], Will Woodgate[7], Jason Beringer[8], Kerry Cawse-Nicholson[9], Siyan Ma[3], Joseph Verfaillie[3], Dennis Baldocchi[3]

[1]Agriculture &Land Ecosystem Division, Space Applications Center, ISRO, Ahmedabad, India
[2]Remote Sensing and Natural Resources Modeling, Department ERIN, Luxembourg Institute of Science and Technology, Belvaux, Luxembourg
[3]Environemtal Science Policy and Management, University of California, Berkeley, United States
[4]Centre for Atmosphere and Oceanic Studies, Indian Institute of Sciences, Bengaluru, India
[5]Centre for Ecology and Hydrology, Lancaster, UK
[6]Terrestrial Ecosystem Research Network, College of Science and Engineering, James Cook University, Cairns, Queensland
[7]CSIRO Land and Water, Private Bag 5, Floreat 6913, Western Australia.
[8]School of Earth and Environment, The University of Western Australia, WA, 6009, Australia
[9]Carbon Cycles and Ecosystems, Jet Propulsion Laboratory, California Institute of Technology, United States
[10]Department of Physics, Electronics & Space Sciences, Gujarat University, Ahmedabad, India
[11]Department of Physics, Institute of Science, Silver Oak University, Ahmedabad, Gujarat, India

Corresponding authors: Kaniska Mallick (kaniska.mallick@gmail.com) and Devansh Desai (ddesai10793@gmail.com)

[#]Contributed equally to revision

Abstract

One of the major undetermined problems in evaporation (ET) retrieval using thermal infrared remote sensing is the lack of a physically based ground heat flux (G) model and its integration with the surface energy balance model. Here, we present a novel approach based on coupling a thermal inertia (TI)-based mechanistic G model with an analytical surface energy balance model, Surface Temperature Initiated Closure (STIC, version STIC1.2). The coupled model is named STIC-TI and it uses noon-night (1:30 pm and am) land surface temperature (T_S), surface albedo, and vegetation index from MODIS Aqua in conjunction with a clear-sky net radiation model and ancillary meteorological information. SEB flux estimates from STIC-TI were evaluated with respect to the *in-situ* fluxes from Eddy Covariance measurements in diverse ecosystems of contrasting aridity in both northern and southern hemispheres. Sensitivity analysis revealed substantial sensitivity of STIC-TI-derived fluxes due to T_S uncertainty. An evaluation of noontime G (G_i) estimates showed 12-21% error across six flux tower sites in both the hemispheres and a comparison between STIC-TI versus other G models also revealed the substantially better performance of the former. While the instantaneous noontime net radiation (R_{Ni}) and latent heat flux (LE_i) was overestimated (15% and 25%), sensible heat flux (H_i) was underestimated (22%). The errors in G_i were associated with the errors in daytime T_S and mismatch of footprint between the model estimates and measurements. Overestimation (underestimation) of LE_i (H_i) was associated with the overestimation of net available energy ($R_{Ni} – G_i$) and use of unclosed surface energy balance measurements. The deviations of STIC-TI heat flux estimates from measurements were found to be restricted within -40° to 30° day view angle, while no impact of night view angle was evident. Being independent of any leaf-scale parameterization and having a coupled sub-model of G, STIC-TI can make a valuable contribution to mapping and monitoring ecosystem water stress and evaporation using noon-night thermal infrared observations from existing and future EO missions such as INSAT 4th generation and TRISHNA.

Keywords: Thermal remote sensing, water stress, evaporation, ground heat flux, thermal inertia, surface energy balance, STIC, terrestrial ecosystem

1 Introduction

One of the outstanding challenges in evaporation (ET) estimation through surface energy balance (SEB) model concerns an accurate characterization of ground heat flux in the open canopy system with mixed vegetation such as savanna or in ecosystems with low mean fractional vegetation cover, prevailing water stress, and strong seasonality in soil moisture. Ground heat flux (G) is an intrinsic component of SEB (Sauer and Horton, 2005), affecting the net available energy for ET (the equivalent water depth of latent heat flux, LE) and sensible heat flux (H). It represents an energy flow path that couples surface with the atmosphere and has important implications for the underlying thermal regime (Sauer and Horton, 2005). Depending on the vegetation fraction and water stress, the magnitude of instantaneous G varies greatly across different ecosystems. In the humid ecosystems with predominantly dense canopies and high mean fractional vegetation cover, G contributes to a small proportion in the surface energy balance. Dense canopy cover leads to less transmission of radiative fluxes through multiple layers of canopies, which results in low warming of the soil floor. Due to persistently high soil water content, humid ecosystems generally show low diurnal and seasonal variability in G. By contrast, the magnitude of G is substantially large in arid and semi-arid ecosystems with sparse and open canopy and soil moisture deficits. Due to prevailing feedback between the physics of ground heat flux, land-atmosphere interactions and vegetation ecophysiology, evaporation modelling in the complex ecosystems remained a challenging task (Wang et al., 2013; Kiptala et al., 2013). This paper addresses the challenge of simultaneous estimation of G and ET by combining thermal remote sensing observations with a mechanistic G model and a SEB model.

SEB models mainly emphasize on estimating sensible heat flux (H) by resolving the aerodynamic conductance (g_A) and computes LE as a residual SEB component as follows:

$$LE = R_N - G - H \quad (1)$$

R_N is the net radiation. The proportion of R_N that is partitioned into G depends upon soil properties like its albedo, soil moisture, soil thermal properties such as thermal conductivity and heat capacity, which vary with mineral, organic and soil water fractions. SEB models use land surface temperature (LST or T_S) as an important lower boundary condition for estimating H and LE. Due to the extraordinarily high sensitivity of T_S to evaporative cooling and soil water

content variations, thermal infrared (TIR) remote sensing is extensively used in large scale evaporation diagnostics (Kustas and Anderson, 2009; Mallick et al., 2014, 2015a, 2018a; Cammalleri and Vogt, 2015; Anderson et al., 2012). Evaporation estimation through SEB models commonly employ empirical sub-models of G in a stand-alone mode. Despite the utility of mechanistic G models is demonstrated in different studies (Verhoef, 2004; Murray and Verhoef, 2007; Verhoef et al., 2012), no TIR-based evaporation study attempted to couple a mechanistic G model with a SEB model.

The SEB models for ET estimation driven by remote sensing observations generally use linear and non-linear relationships for estimating G and such methods generally employ R_N, T_S, albedo (α_R), and NDVI (e.g., Bastiaanssen et al., 1998; Friedl, 2002; Santanello and Friedl, 2003). While the inclusion of T_S and albedo serves as a proxy for soil moisture and surface characteristics effects in G, inclusion of NDVI provides a scaling of G - R_N ratio for different fractional vegetation cover. Unfortunately, the empirical approaches do not include any information of soil temperature or daily temperature amplitude. These empirical models also lack the universal consensus. Setting G as a fraction of R_N does not solve the energy balance equation and disregards the role of thermal inertia of the land surface (Mallick et al., 2015b). This could introduce substantial uncertainty in LE estimation because G effectively couples the surface energy balance with energy transfer processes in the soil thermal regime. It provides physical feedback to LE through the effects of soil moisture, temperature, and conductivity (thermal and hydraulic) (Sauer and Horton, 2005). Such feedbacks are most critical in the arid and semi-arid ecosystems where LE is significantly constrained by the soil moisture dry-down. The limits imposed on LE by the water stress consequently result in greater partitioning of the net available energy (i.e., $R_N - G$) into H and G (Castelli et al., 1999).

When LE is reduced due to soil moisture dry-down, both G and T_S tend to show rapid intra-seasonal rise. Therefore, the surface energy balance equation could be linked with mechanistic G model, T_S harmonics (Verhoef, 2004), and soil moisture availability. Realizing the importance of direct estimates of G in LE and invigorated by the advent of TIR remote sensing, Verhoef et al. (2012) demonstrated the potential of a TI-based mechanistic model (Murray and Verhoef, 2007) (MV2007 hereafter) for spatiotemporal G estimates in semi-arid ecosystems of Africa. Some studies also emphasized the importance of using noontime and nighttime Ts and R_N for

117 estimating G (Mallick et al., 2015b; Bennet et al., 2008; Tsuang, 2005). The method of MV2007
118 has so far been tested in a stand-alone mode, and no remote sensing method has so far been
119 attempted to combine such a mechanistic G model (e.g., MV2007-TI model) with a SEB model
120 for coupled energy-water flux estimation and validation.

121 By integrating T_S into a combined structure of the Penman-Monteith (PM) and Shuttleworth-
122 Wallace (SW) model, an analytical SEB model was proposed by Mallick et al. (2014, 2015a,
123 2016). The model, Surface Temperature Initiated Closure (STIC), is based on finding analytical
124 solution for aerodynamic and canopy-surface conductance (g_A and g_S) where the expressions of
125 the conductances were constrained by an aggregated water stress factor. Through physically
126 linking water stress (T_S derived) with g_A and g_S, STIC established direct feedback between T_S, H
127 and LE, and simultaneously overcame the need of empirical parameterization for estimating the
128 conductances (Mallick et al., 2016, 2018a). Different versions of STIC have been extensively
129 validated in different ecological transects (Tropical rainforest to woody savanna) and aridity
130 gradients (humid to arid) (Trebs et al., 2021; Bai et al., 2021; Mallick et al., 2015a; 2016; 2018a,
131 b; Bhattarai et al., 2018, 2019). Based on the conclusions of Verhoef et al. (2012), Mallick et al.
132 (2014; 2015a,b; 2016; 2018a,b, 2022), Bhattarai et al. (2018, 2019), and Bai et al. (2021), there
133 is a need to address some of the challenges in SEB modeling, which are, (i) accurate estimation
134 of G and ET in sparse vegetation, (ii) testing the utility of coupling a TI-based G model with an
135 analytical SEB model for accurately estimating G and ET, and (iii) detailed evaluation of a
136 coupled G-SEB model at the ecosystem scale. Realizing the significance of mechanistic G model
137 (MV2007), the advantage of the analytical STIC model, and to mitigate some of the overarching
138 gaps in SEB modeling in sparsely vegetated open canopy systems, this study presents the first-
139 ever coupled implementation of MV2007 G with the most recent version of STIC (STIC1.2). We
140 name this new coupled model as STIC-TI and it requires noon-night Ts and associated remotely
141 sensed land surface variables as inputs. We performed subsequent evaluation of STIC-TI in nine
142 terrestrial ecosystems in arid, semi-arid and sub-humid climate in India, the United States of
143 America (USA) (representing northern hemisphere) and Australia (representing southern
144 hemisphere) at the eddy covariance flux tower sites. The current study addresses the following
145 research questions and objectives:

(i) What is the performance of STIC-TI G estimates when compared with conventionally used empirical G models in ecosystems having low mean fractional vegetation cover (f_c) (≤0.5) and having larger soil exposure to radiation for example in Savanna?

(ii) How do the estimates from STIC-TI LE and H fluxes compare with LE and H observations in diverse terrestrial ecosystems that represent a varied range of f_c (0.25 – 0.5) covering cropland, savanna, mulga vegetation (woodlands and open-forests dominated by the mulga tree [*Acacia aneura*]) spread across arid, semi-arid, sub-humid, humid climates over a vast range of rainfall (250 to 1730 mm), temperature (-4 to 46°C) and soil regimes?

(iii) What is the seasonal variability of G and evaporative fraction from STIC-TI model in a wide range of ecosystems having contrasting aridity and vegetation cover?

It is important to mention that assessing the performance of STIC-TI LE and H with respect to other SEB models is not within the scope of the present study. The prime focus of the current study is to assess the sensitivity of STIC-TI, temporal variability of the retrieved SEB fluxes, and cross-site validation of the individual SEB components.

A list of variables, their symbols and corresponding units are given in Table A1 in Appendix A.

2 Study area and datasets

2.1Study site characteristics

The present study was conducted using data from nine flux tower sites (four sites in India; three sites in Australia; two sites in USA) equipped with Eddy Covariance (EC) measurement systems. The distribution of the flux tower sites considered for the present study are shown in Fig.1 below. The sites cover a wide range of climate, vegetation types, low fractional vegetation cover (f_c) of around 0.5 and have contrasting aridity (Table 1). In India, a network of EC towers was set up under Indo-UK INCOMPASS (INteraction of Convective Organization and Monsoon Precipitation, Atmosphere, Surface and Sea*)* Program (Turner et al., 2019) at Jaisalmer (IND-Jai) in Rajasthan state, Nawagam (IND-Naw) in Gujarat state, Samastipur (IND-Sam) in Bihar state and under Newton-Bhaba programme (Morisson et al., 2019 a,b) at Dharwad (IND-Dha) in Karnataka state. The flux footprint for EC towers in India varied from 500 m – 1 km (Bhat et al., 2019). In the present study, about 90% of the fluxes came from an area within 500 m to 1 km

from the EC tower. Therefore, the relative contribution of vegetated land surface area to the fluxes is close to 90% (Schmid, 2002; Vesala et al., 2008). The remaining percentage of fluxes were originated from an area beyond the flux footprint. The mean annual f_c was found to vary from 0.25 to 0.52 with standard deviation (SD) ranging from 0.1 to 0.16.

The IND-Jai site represents arid western zone over desert plains of natural grassland ecosystem. The region receives very low rainfall (100 – 300 mm) during monsoon and experiences a wide range in air temperature, high solar radiation, wind speed and high evaporative demand (Raja et al., 2015). The IND-Naw site represents semi-arid agroecosystem in the middle Gujarat agroclimatic zone of north-west India and has a pre-dominant rice-wheat cropping system. The IND-Sam site has sub-humid climate of north-west alluvial plain zone in the Indo-Gangetic Plain (IGP) situated in the eastern India and this site also follows rice-wheat crop rotation. IND-Dha represents humid sub-tropical climate of transition zone in the southern India and this site comprises of crops.

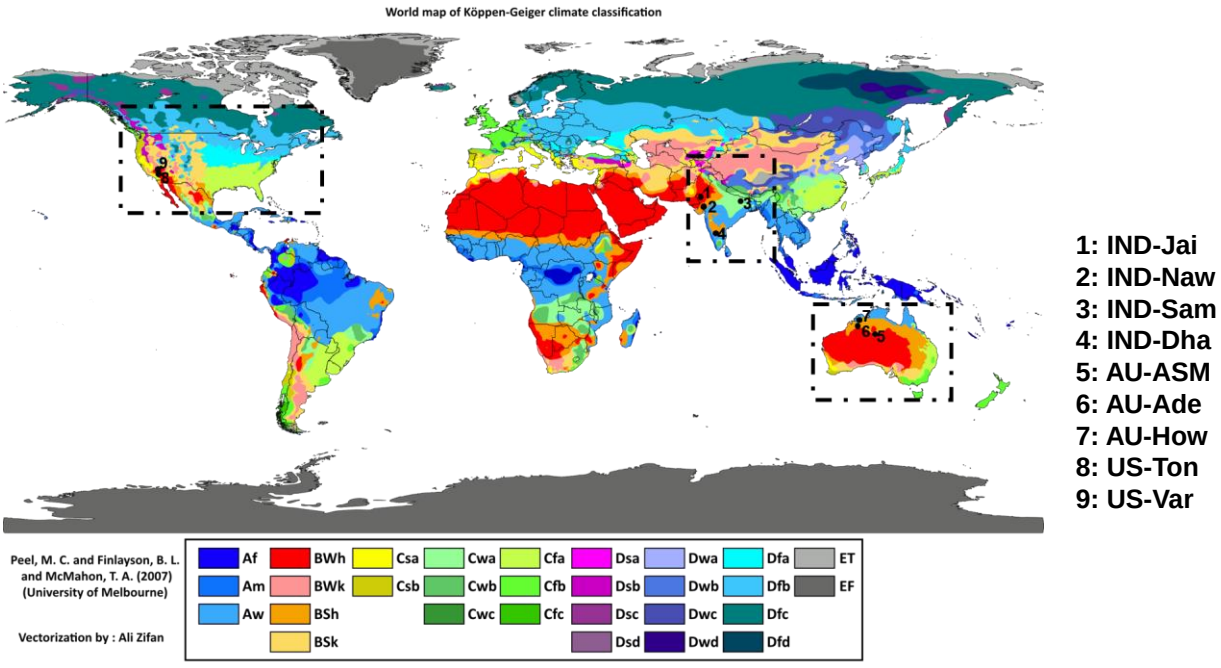

Figure 1: Locations of the flux tower sites in India, Australia and USA overlaid on climate type map. (Image Source: By Peel, M. C., Finlayson, B. L., and McMahon, T. A. (University of Melbourne) enhanced, modified, and vectorized by Ali Zifan; Hydrology and Earth System Sciences: "Updated world map of the Köppen-Geiger climate classification". Legend explanation, CC BY-SA 4.0, https://commons.wikimedia.org/w/index.php?curid=47086879)

In USA, two EC tower sites were located at Tonzi Ranch (US-Ton) and Vaira Ranch (US-Var), in the lower foothills of the Sierra Nevada Mountains. Both the EC stations are part of the AMERIFLUX Management Project (https://ameriflux.lbl.gov/). US-Ton is classified as an oak savanna woodland. While the overstorey is dominated by blue oak trees (40% of total vegetation) with intermittent grey pine trees (3 $treesha^{-1}$), the understory species include a variety of grasses and herbs. The mean annual rainfall at this site is 559 mm. US-Var isa grassland dominated site and the growing season is confined to the wet season only, typically from October to early May. The mean annual rainfall at this site is 559 mm. The mean annual f_c was found to vary from 0.18 to 0.26 and SD of the order of 0.06 to 0.07.

In Australia, three EC tower sites were located at Howard Springs (AU-How), Alice Springs Mulga (AU-ASM), Adelaide river (AU-Ade) in the Northern Territory as part of the OzFlux network (Beringer et al., 2016) and the Terrestrial Ecosystem Research Network (TERN), which is supported by the National Collaborative Infrastructure Strategy (NCRIS) (http://www.ozflux.org.au/monitoringsites/index.html). The AU-How is situated in the Black Jungle Conservation Reserve representing an open woodland savanna and the mean annual rainfall is 1750 mm. The AU-ASM is located on Pine Hill cattle station near Alice Springs. The woodland is characterized by mulga canopy and mean annual rainfall is 306 mm. AU-Ade represents savanna with a mean annual rainfall of 1730 mm. The mean annual f_c varied from 0.21 to 0.48 having SD range of 0.08 - 0.17. A description of Australian flux sites is given in Beringer et al. (2016). Average heights of vegetation are 1.15 m at IND-Naw, 1 m at IND-Jai, 1.23 m at IND-Sam, 1.5 m at IND-Dha, 6.5 m at AU-ASM, 15m at AU-How, 7 m at AU-Ade, 10 m at US-Ton, and $\leq$ 0.5 m at US-Var.

Table 1: An overview of the EC flux tower site characteristics in the present study

Hemisphere	Sites	Latitude (°N), Longitude (°E)	Climate & Vegetation	Mean f_c (SD)	Soil texture	T_A range (°C)	Mean Annual P (mm)	Observation period
Northern	Jaisalmer (IND-Jai)	26.99, 71.34	Arid grassland	0.25(±0.1)	Loamy fine sand to coarse sand	8 – 40	250	2017 – 2018
	Nawagam (IND-Naw)	22.80, 72.57	Semi-arid cropland	0.41(±0.13)	Sandy loam	9 – 39	700	2017 – 2018
	Samastipur (IND-Sam)	26.00, 85.67	Humid subtropical cropland	0.52(±0.16)	Sandy loam to loam	10 – 39	1000	2017 – 2018
	Dharwad (IND-Dha)	15.50, 74.99	Tropical Savanna	0.36(±0.11)	Shallow to medium black clay and red sandy loam soils	12 – 40	650	2016 – 2018
	Tonzi ranch (US-Ton)	38.43, -120.96	Woody Savanna	0.18(±0.06)	Red sandy clay loam	0 – 40	559	2011 – 2019
	Vaira ranch (US-Var)	38.41, -120.95	Arid grassland	0.26(±0.07)	Rocky silt loam	0 – 40	559	2011 – 2019
Southern	Alice Springs Mulga (AU-ASM)	-22.28, 133.24	Semi-arid mulga	0.21(±0.09)	Loamy sand	(-4) – 40	305	2011 – 2014
	Howard Springs (AU-How)	-12.49, 131.15	Tropical savanna	0.48(±0.17)	Red kandasol	19 – 34	1700	2011 – 2014
	Adelaide River (AU-Ade)	-13.07, 131.11	Savanna	0.42(±0.08)	Yellow hydrosol, shallow, loamy sand with coarse gravel	16 – 37	1730	2007 – 2009

T_A: Air temperature during the observation period; P: rainfall (mm) measured using rain gauge at flux tower site during the study period. IND is for India, AU is for Australia, and US is for the United States; SD is standard deviation of annual mean fc which is computed from NDVI as mentioned in section 3.1.

2.2Datasets

2.2.1Micrometeorological data at flux tower sites

Standardized, controlled and harmonized surface energy balance (SEB) flux and meteorological data from nine EC towers were used in the present analysis. In Australia, H and LE were measured through the EC systems and R_N were measured through net radiometers at varying heights of 15 m (AU-Ade), 23 m (AU-How), and 11.6 m (AU-ASM), respectively. In India, the EC measurement height was maintained approximately at 8 m above the surface, except at IND-Dha where it was installed at a height of 4.2 m. In USA, the SEB measurements were carried out at tower heights of 23 m at US-Ton and 2 m US-Var. A summary of the instrumentation is given in Table A2 of Appendix A. All the flux tower sites were equipped with a range of meteorological instrumentation which measured diurnal air temperature (T_A) and relative humidity (R_H), four components of the net radiation (R_N, consisting of down- and up-welling shortwave and long-wave radiation (SW↓, SW↑, LW↑ and LW↓, respectively)) above the vegetated canopy. In addition, the diurnal soil heat flux (G) and soil temperature (T_{ST}) were measured at all the three Australian sites and two US sites. In India, the diurnal soil heat flux was measured only at IND-Dha.

For the Indian sites, the raw EC measurements of the turbulent wind vectors (*u*, *v* and *w*, for horizontal, meridional and vertical, respectively), sonic temperature (T), and CO_2 and water vapor mass density were recorded at a sampling rate of 20 Hz. Raw EC data were post-processed to obtain level-3 quality controlled and harmonized surface fluxes at 30-minute flux averaging intervals using EddyPRO® Flux Calculation Software (LI-COR Biosciences, Lincoln, Nebraska, USA) using the data handling protocol described by Bhat et al. (2019). The EC data from the OzFlux sites was averaged over 30 minutes recorded by the logger and processed through levels using the PyFluxPro standard software processing scripts as mentioned in Isaac et al. (2017). The Level 3 (L3) used in this paper was produced using PyFluxPro (Isaac et al., 2017) employing the Dynamic INtegrated Gap filling and partitioning for Ozflux (DINGO) system as described in Donohue et al. (2014) and Beringer et al. (2016).The quality checked EC data at 30 minute intervals for two AMERIFLUX sites US-Ton and US-Var was acquired from *https://doi.org/10.17190/AMF/1245971&https://doi.org/10.17190/AMF/1245984*, respectively.

2.2.2 Remote sensing data

Optical and thermal remote sensing observations available from Moderate Resolution Imaging Spectroradiometer (MODIS) (Didan et al., 2015) on-board Aqua platform were used in the present study (Table 2) for estimating G and associated SEB fluxes. These include eight-day land surface temperature (LST or T_S) at 1:30 pm and 1:30 am, and surface emissivity (ε_s) (MYD11A2), daily surface albedo (α_R) (MCD43A3), 16-day NDVI (MYD13A2). The overpass times of MODIS Aqua are at 1:30 pm and 1:30 am. The 8-day average values of clear-sky T_S available from MYD11A2 data were used (Source: https://vip.arizona.edu/documents/viplab/MYD11A2.pdf) for all nine flux tower sites. Since MYD21A2 LST product is known to provide better accuracy (1 – 1.5 K) (Hulley et al, 2016) as compared to MYD11A2 LST over semi-arid and arid ecosystems, the former was also used in STIC-TI to compare LE and H estimates (see Table 5 in section 4.4) with the estimates of MYD11A2 LST over the arid and semi-arid sites (IND-Jai, IND-Naw, US-Ton). The noon-night pair of thermal remote sensing observations from Aqua are close to the time of occurrences of maximum and minimum soil surface temperature (see Figure 2) and are therefore ideal for soil heat flux modeling using thermal inertia. The MODIS Terra overpass times are at 11 am and 11 pm and are far from the time of occurrences of minimum-maximum soil temperatures. Therefore, MODIS Aqua acquisition times were used in the present study.

Table 2: A summary of MODIS Aqua optical and thermal remote sensing products used in the present study

Data type	Product ID (version)	Variables used	Spatial resolution (m)	Temporal resolution	Purpose	Inputs to equation numbers
LST and emissivity	MYD11A2 (V006) MYD21A2	T_S (1:30 pm and am) and ε_s	923	8-day	For estimating R_{Ni}, G_i, LE_i, H_i	(5), (13), (C6), (C7), (B8)
Surface albedo	MCD43A3 (V006)	α_R	462	8-day composite from daily	For estimating R_{Ni},G_i	(5), (B3)

Vegetation index	MYD13Q1 (V006)	NDVI	250	16-day	For estimating G_i	(4)

3 Methodology

3.1 Coupled soil heat flux-SEB model

In this paper, we modified a thermal inertia (TI) based soil heat flux (G) model using noon-night thermal remote sensing observations and thereafter coupled the TI-based G with STIC1.2. A clear-sky net radiation (R_N) model was also introduced into this coupled model and R_N estimation algorithm is described in Appendix B. The estimation of G through modifying MV2007-TI approach and its coupling with STIC1.2 is the most novel component of the modeling scheme, and it is therefore described in the main body of the paper (section 3.1.1). Such a coupling enabled the implementation of a mechanistic G model along with an analytical SEB model using optical-thermal remote sensing data. The coupled model is hereafter referred as STIC-TI.

3.1.1 MV2007 soil heat flux model based on Thermal Inertia (TI)

The functional form for estimating instantaneous G (G_i, hereafter) (eq. 2 below) is based on the harmonic analysis of soil surface temperature and is described in detail by Murray and Verhoef (2007) and Maltese et al. (2013).

$$G_i = \Gamma\left[(1-0.5f_C)\left(\sum_{n=1}^{k} A\sqrt{n\omega}\sin\left(n\omega t + \phi'_n + \frac{\pi}{4} - \frac{\pi\Delta t}{12}\right)\right)\right] = \Gamma J_S \qquad (2)$$

G_i is the soil heat flux at the surface at a particular instance (Wm^{-2}), Γ is the soil thermal inertia ($J\ m^{-2}\ K^{-1}\ s^{-0.5}$), k is the total number of harmonics used, A is the amplitude (°C) of the n^{th} soil surface temperature (T_{ST}) harmonic, ω is the angular frequency ($rads^{-1}$), t is the time (s), ϕ'_n is the phase shift of the n^{th} soil surface temperature harmonic (rad), J_S is the summation of harmonic terms of soil surface temperature (K), and Δt(s) is time offset between the canopy composite temperature and the below-canopy soil surface temperature. Here, we represent G_i and A as ecosystem-scale (≤ 1km) soil heat flux and surface soil temperature amplitude (averaged from

soil surface to 10 cm depth), respectively and assume it to be valid for different vegetated landscape.

Since we have considered a single pair (noon-night corresponding to 1:30 pm and 1:30 am) of MODIS aqua LST data in the present study, the phase shift (ϕ'_n) is taken as zero and number of harmonics is taken as one (k=1) for estimating G_i. Thus equation (2) is modified as follows:

$$G_i = \Gamma\left[(1 - 0.5f_C)\left(A\sqrt{\omega}\sin\left(\omega t' + \frac{\pi}{4} - \frac{\pi\Delta t}{12}\right)\right)\right] = \Gamma J_S \quad (3)$$

Δt(s) is found to be 1.5 h (Murray and Verhoef, 2007). With the two boundary values (i.e., Δt =1.5 h for $f_c = 1$ and $\Delta t = 0$ for $f_c = 0$), a linear approach is proposed here to describe the time offset Δt as a function of vegetation fraction (f_c) (Murray and Verhoef, 2007; Maltese et al., 2013). f_c was derived from NDVI on a given day or period and from the upper-lower limits of annual NDVI cycle.

$$\Delta t = 1.5\, f_c \quad (4)$$

3.1.1.1 Scaling function for estimating ecosystem-scale surface soil temperature amplitude (A)

Estimating ecosystem-scale A involves two steps, (a) computing point-scale soil surface temperature amplitude (from surface to 0.1m depth) ($T_{STA,}$ hereafter) from the available measurements of soil surface temperature, and (b) linking T_{STA} with remote sensing variables to develop scaling functions for A. Point-scale soil temperature measured at different depths within top 10 cm soil layer at AU-ASM, US-Ton, US-Var was averaged and considered as representative surface soil temperature (0 – 10 cm). For Ind-Dha and AU-Ade, single-depth (10 cm) soil temperature measurement was used. Studies also showed that LST carries some signal beneath the skin of the surface (Johnston et al., 2022).

Several studies suggested theoretical sinusoidal trajectory of soil surface and sub-surface temperatures (Gao et al., 2010), where the amplitude is maximum at the surface, and it gradually decreases with depth to become 37% of surface amplitude until the damping depth (Hillel, 1982). However, at deeper depths, soil temperatures remain constant with time and do not show many fluctuations as compared to surface or near-surface soil temperatures. This invariant soil temperature is called deep soil temperature (Mihailovic et al., 1999). However, the diurnal

surface soil temperature measurements (within top 0.1 m depth) across different flux tower sites showed a sinusoidal-exponential behavior, i.e., sinusoidal pattern from sunrise until the afternoon and exponential pattern from afternoon through sunset to the next sunrise. An illustrative example of the theoretical and observed trajectories of surface soil temperature is shown in Fig. 2. This diurnal surface soil temperature variation has a single harmonic component (Gao et al., 2010). For computing T_{STA}, theoretical half-curve of sinusoidal pattern is assumed and was derived from measurements as exemplified in Fig 2.

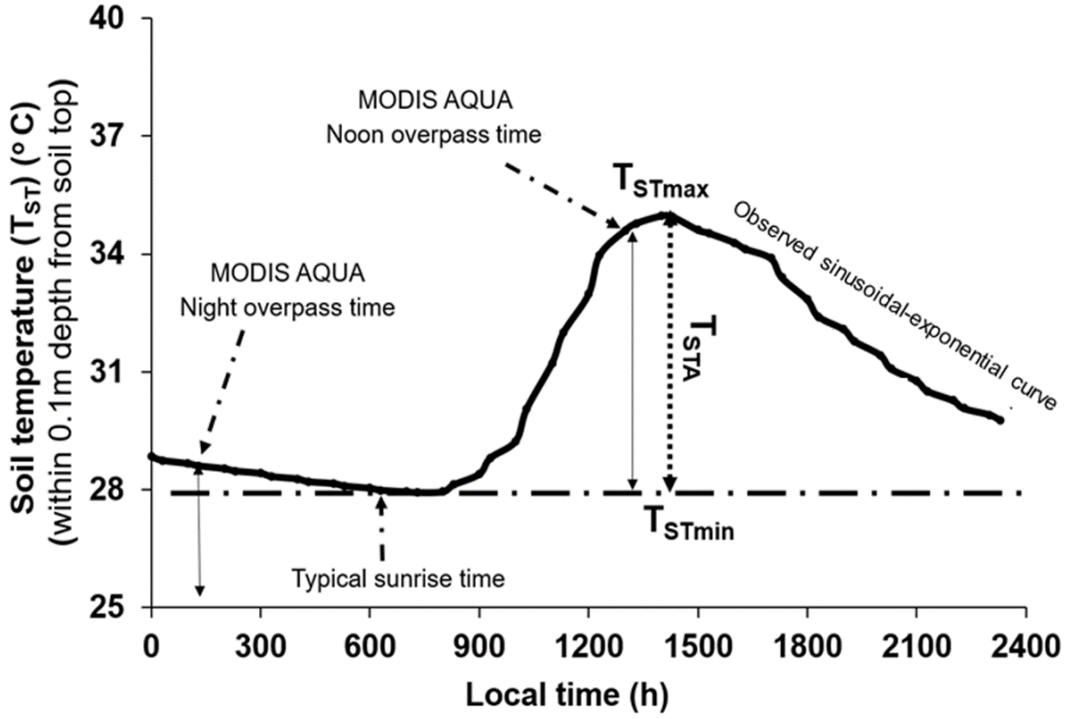

Figure 2. An illustrative example of typical diurnal variation of observed soil temperature (T_{ST}) (from surface to 0.1m depth) at OzFlux sites and timings of MODIS AQUA observations. Here, T_{STmax} and T_{STmin} are maximum and minimum point-scale observed soil surface temperatures

It is evident from Fig. 2 that T_{STmin} represents minimum surface soil temperature occurring 1-1.5h after sunrise and T_{STmax} occurs during 12.30 – 15.00h local time. The *in-situ* measured T_{ST} on completely clear-sky days at OzFlux sites were used to extract T_{STmax} and T_{STmin} and T_{STA} was derived as (T_{STmax}- T_{STmin}) from the theoretical half-curve of sinusoidal pattern.

T_{STA} is generally influenced by several land surface characteristics such as surface temperature and surface albedo of soil-canopy complex, surface heat capacities, fractional canopy cover and

thermal conductivity (White, 2013). T_S and α_R are the major thermal and reflective land surface properties that have strong synergy with surface soil temperature dynamics. Hence, we have used bivariate regression analysis to develop a scaling function for estimating ecosystem-scale T_{STA} (top to 0.1m depth). The bivariate regression is based on the difference of noon (d) and night (n) T_S data andα_R (Duan et al., 2013, Li Tian et al., 2014) from MODIS Aqua. The scaling function given in eq. (5) estimates ecosystem-scale T_{STA} (symbolized as 'A' in equation 5) from surface to 0.1 m soil depth:

$$A = B_1(T_{Sd} - T_{Sn}) + B_2(\alpha_R) + B_3 \quad (5)$$

Here, B1, B2, B3 are coefficients of regression model; T_{Sd} and T_{Sn} are noon and nighttime LST, respectively. The results of this regression analysis are elaborated in section 4.1.

3.1.1.2 Estimating Γ

Γ is the key variable for estimating G_i using eq. (2). MV2007 adopted the concept of normalized thermal conductivity (Johansen, 1975) and developed a physical method to estimate Γ as follows:

$$\Gamma = e^{\left[\Upsilon'\left(1 - S_r^{(\Upsilon' - \delta)}\right)\right]}(\tau_* - \tau_0) + \tau_0 \quad (6)$$

where τ_* and τ_0 are the thermal inertia for saturated and air-dry soil (J $m^{-2}K^{-1}s^{-0.5}$); $\tau_0 = D_1\theta_* + D_2$; $\tau_* = D_3\ (\theta_*^{-1.29})$; Υ' (−) is a parameter depending on the soil texture (Murray and Verhoef, 2007; Minasny, 2007; Anderson et al., 2007); S_r (m^3 m^{-3}) is relative saturation and is equal to (θ/θ_*); δ (unitless) is the shape parameter which is dependent on the soil texture. θ_* (m^3 m^{-3}) is the soil porosity (equal to the saturated soil moisture content when soil moisture suction is zero), θ (cm^3 cm^{-3}) is the volumetric soil moisture and D_1, D_2, D_3 are coefficients which were derived from a large number of experimental data. The reported global values of D_1, D_2, and D_3 were taken as -1062.4, 1010.8, 788.2, respectively (Maltese et al., 2013). The value for θ_* and shape parameter for soil textures across study sites were specified according to Van Genuchten et al. (1980). The details are mentioned in Table E1 of Appendix E.

In the present study, the relative soil moisture saturation, $S_r(\theta/\theta_*)$ is represented in terms of an aggregated moisture availability (M) of canopy-soil complex through a linear function (eq. 12).

In case of zero canopy cover, M represents the soil moisture availability from surface to 0.1 m depth. In sparse and open canopy, rates of moisture availability from soil to root and root to canopy were assumed same.

Theoretically, M is expressed as available soil moisture fraction between field capacity (θ_{fc}) and permanent wilting (θ_{wp}) point as given in eq. (7) below.

$$M = \frac{\theta - \theta_{wp}}{\theta_{fc} - \theta_{wp}} \tag{7}$$

Where, θ_{fc} ($m^3\ m^{-3}$) is the volumetric soil moisture at the field capacity (at a suction of 330 hPa) and θ_{wp} ($m^3\ m^{-3}$) is the volumetric soil moisture at the permanent wilting point (at suction of 15000 hPa) (Singh, 2007). Since θ_{fc}, θ_*, θ_{wp} are characteristic volumetric soil moisture contents corresponding to specific suctions and depends on the soil texture, dividing the numerator and denominator in eq. (7) by θ_* gives the following expression:

$$M = \frac{\frac{\theta}{\theta_*} - \frac{\theta_{wp}}{\theta_*}}{\frac{\theta_{fc}}{\theta_*} - \frac{\theta_{wp}}{\theta_*}} \tag{8}$$

Due to their dependence on soil texture, the ratios (θ_{fc}/θ_*) and (θ_{wp}/θ_*) are treated as constants. These are represented as C and C′ in the later equations (eq. 9, 10, and 11). The constants, C and C′ vary from 0.3 to 0.8 and from 0.1 to 0.4 (Murray and Verhoef, 2007; Minasny et al., 2011; Anderson et al., 2007), respectively over different soil textures.

$$M = \frac{\frac{\theta}{\theta_*} - C'}{C - C'} \tag{9}$$

$$M(C - C') = \left(\frac{\theta}{\theta_*}\right) - C' \tag{10}$$

By replacing S_r in eq. (6) as θ/θ_* and by rearranging eq. (10), the following linear function is obtained.

$$S_r = \frac{\theta}{\theta_*} = M\,(C - C') + \quad C' = M' \tag{11}$$

Thus, the modified equation to calculate Γ is given by eq. (12) as follows:

$$\Gamma = e^{\left[\Upsilon'\left(1-M'^{(\Upsilon'-\delta)}\right)\right]}(\tau_* - \tau_0) + \tau_0 \quad (12)$$

By substituting the values obtained from eq. (4), (5) and (12) into eq. (3), we obtained the instantaneous ecosystem-scale G_i corresponding to MODIS Aqua noontime overpass. The intrinsic link between G_i estimates through MV2007-TI and SEB scheme in STIC1.2 is made through M, where the computation of M follows the procedure as described in Mallick et al. (2016, 2018a, b) and Bhattarai et al. (2018). (description in Appendix C).

3.1.1.3 Estimating M

In STIC1.2, an aggregated moisture availability (M) of canopy-soil complex is expressed as the ratio of the 'vapor pressure difference' between the aerodynamic roughness height of the canopy (i.e., source/sink height) and air to the 'vapor pressure deficit' between aerodynamic roughness height to the atmosphere:

$$M = \frac{(e_0 - e_A)}{(e_0^* - e_A)} = \frac{(e_0 - e_A)}{\kappa(e_S^* - e_A)} = \frac{s_1(T_{0D} - T_D)}{\kappa s_2(T_S - T_D)} \quad (13)$$

Where e_0 and e_0^* are the actual and saturation vapor pressure at the source/sink height; e_A is the atmospheric vapor pressure; e_S^* is the saturation vapor pressure at the surface; T_{0D} is dew point temperature at the source/sink height; T_S is the LST; T_D is the air dew point temperature; s_1 and s_2 are the psychrometric slopes of the saturation vapor pressure and temperature between (T_{0D} – T_D) versus (e_0 – e_A) and (T_S – T_D) versus (e_S^* - e_A) relationship; and κ is the ratio between (e_0^* - e_A) and (e_S^* - e_A). To solve the eq. (13), estimation of T_{0D} is necessary. An initial estimate of T_{0D} [$T_{0D} = [(e_S^* - e_A) – s_3T_S + s_1T_D]/(s_1 – s_3)$] and M were obtained following Venturini et al. (2008) where s_1 and s_3 were approximated in T_D and T_S, respectively. However, eq. (13) cannot be directly solved because there are two unknowns in one equation. However, since T_{0D} also depends on LE (Mallick et al., 2016, 2018a), an iterative updation of T_{0D} (and M) was carried out by expressing T_{0D} as a function of LE [$T_{0D} = T_D + (\gamma LE/\rho c_p g_A s_1)$] which is described in detail by Mallick et al. (2016, 2018a) and Bhattarai et al.(2018). In the numerical iteration, s_1 was not updated to avoid numerical instability and it was expressed as a function of T_D.

3.1.2 STIC-TI: Coupling modified MV2007-TI and STIC 1.2

The initiation of the coupling between MV2007-TI and STIC1.2 was executed through linking G_i estimates from the modified MV2007-TI with M estimates from STIC1.2. Having the initial estimates of M (through eq. 13), an initial estimation of G_i was made from eq. (2) where S_r in eq. 11 was replaced with the initial estimates of M'. From the initial estimates of G_i (eq. 2) and R_{Ni} (equations in Appendix B), initial estimates of LE_i and H_i were obtained through the PMEB equation. Analytical expressions of the conductances for estimating H and LE through the PMEB equation were obtained by solving the state equations as described in the Appendix. The process was then iterated by updating T_{0D} [$T_{0D} = T_D + (\gamma LE / \rho c_p g_{AS1})$] and M in every time step (as mentioned in Mallick et al., 2016, 2018a), and re-estimating G_i (using eq. 3), net available energy ($R_{Ni} - G_i$), conductances, LE_i and H_i, until stable estimates of LE_i were obtained. The conceptual block diagram and algorithm flow of STIC-TI is shown in Fig. 3a and Fig 3b, respectively.

(a)

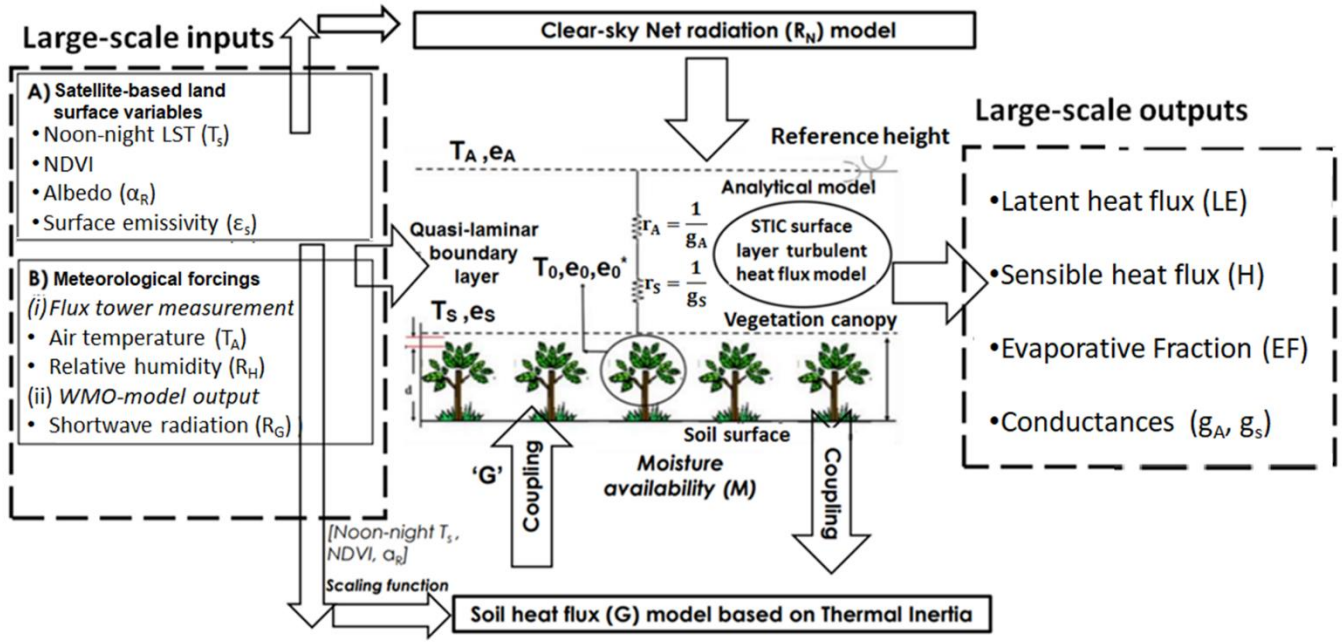

(b)

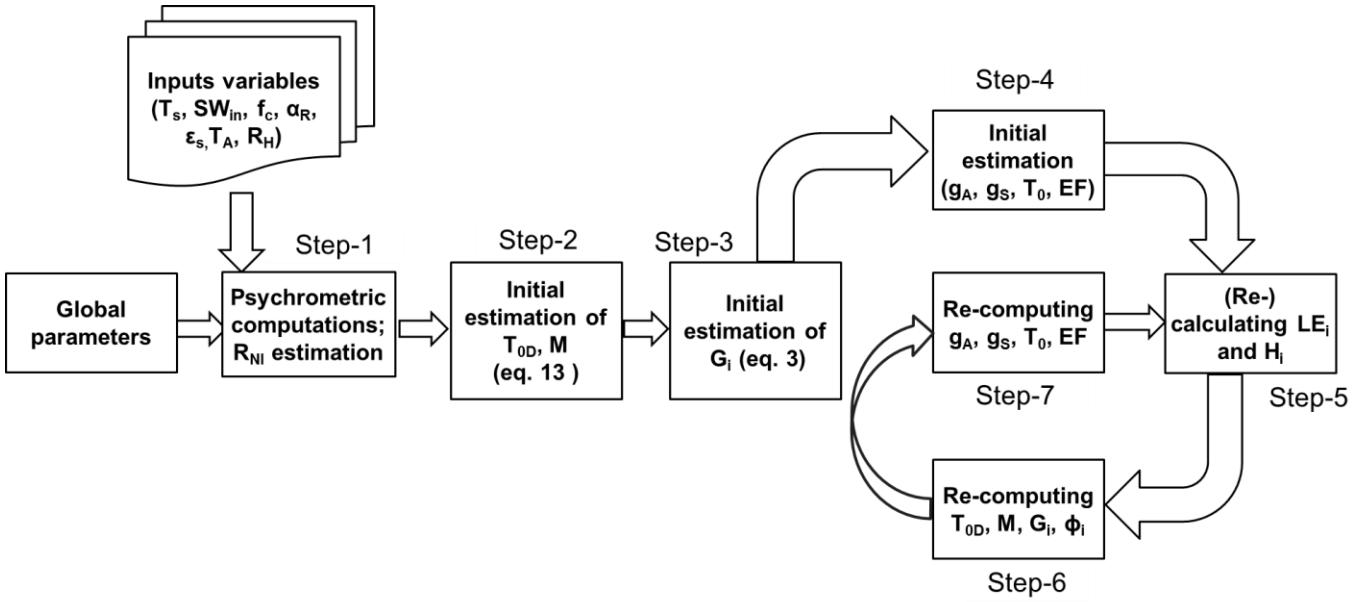

Figure 3: (a) Conceptual diagram of STIC-TI model showing different input variables and model outputs, (b) Algorithmic flow for estimating G and associated SEB fluxes through STIC-TI.

Examples of iterative stabilization of G_i and LE_i for Indian, Australian and US ecosystems of India are shown in Fig. 4. The iterative stabilization of G_i and LE_i was obtained between 8-25 iterations for all sites.

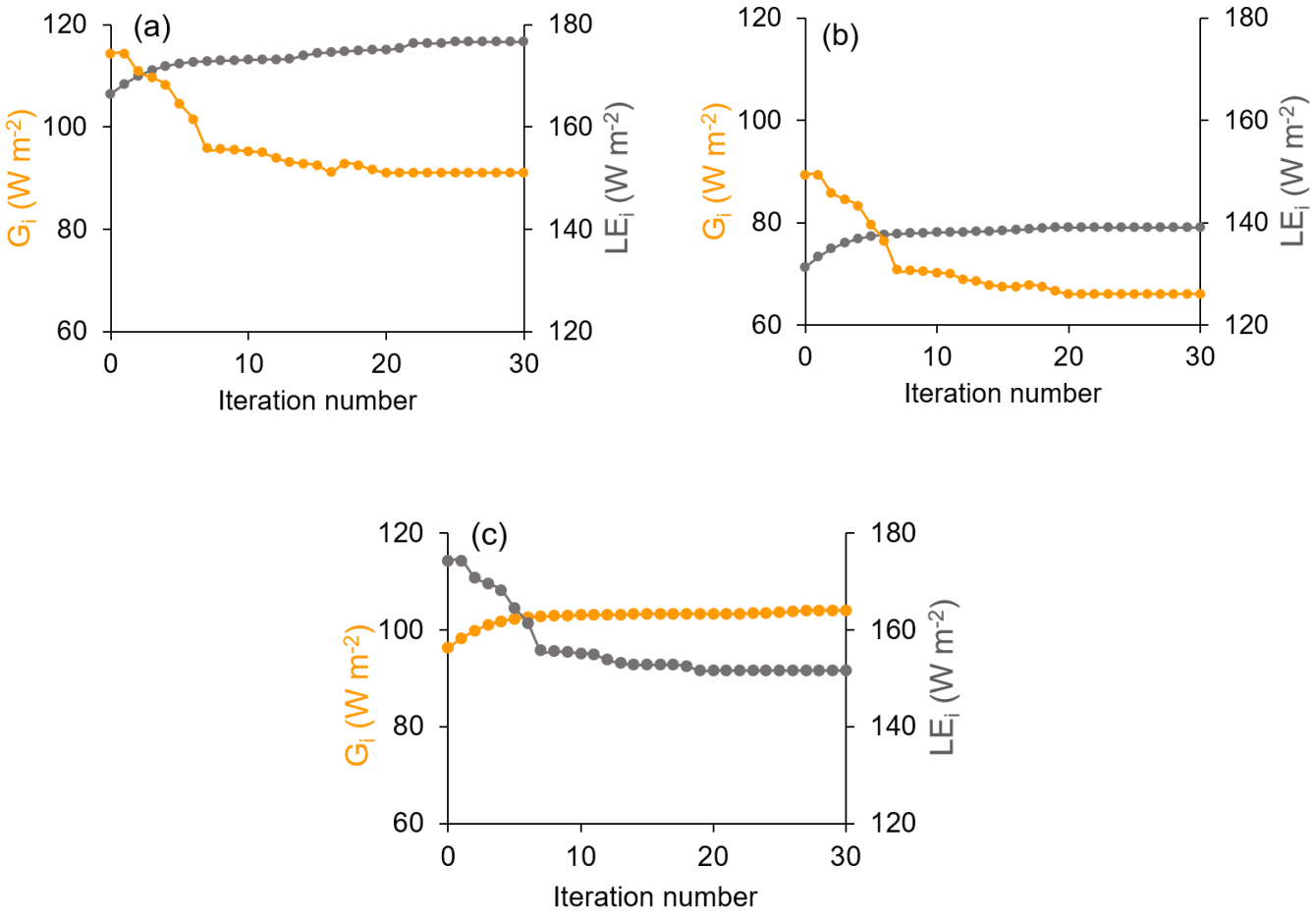

Figure 4: Illustrative examples of iterative stabilization of STIC-TI G_i (yellow marker line) and LE_i (grey marker line) in (a) IND-Jai, (b) AU-ASM, (c) US-Ton

The noteworthy features of STIC-TI are: (1) estimating G by modifying the mechanistic MV2007-TI model using noon and midnight T_S information from thermal remote sensing observations available through polar orbiting satellite platform (e.g. MODIS Aqua), (2) coupling the mechanistic MV2007-TI G model with STIC1.2 to simultaneously estimate surface moisture availability (M), G, and SEB fluxes, (3) introducing water stress information in G (through M) to better constrain the aerodynamic and canopy-surface conductances as well as the SEB fluxes,

and (4) derivation of amplitude of ecosystem-scale surface soil temperature (from top soil to 0.1 m soil depth).

3.1.3 Generation of remote sensing inputs

Two of the key variables in SEB modeling are Ts and ε_s. These two variables were retrieved at 923m spatial resolution from MODIS Aqua noon-night TIR observations (MYD11A2) in bands 11.03 µm and 12.02 µm using a generalized split-window algorithm (Wan et al., 2015). For optimal retrieval, tractable sub-ranges of atmospheric column water vapor and lower boundary air surface temperature were used. Land surface emissivity was estimated from land cover types and anisotropy factors. The MYD21A2 LST product was generated using Temperature-Emissivity Separation (TES) algorithm (Hulley et al, 2016) and improved water vapor scaling method to remove the atmospheric effects. Albedo was estimated from MODIS (MCD43A2 Version 6.0) Bidirectional Reflectance Distribution Function and Albedo (BRDF/Albedo) daily dataset (Schaaf et al., 2002)) at 462 m spatial resolution. Actual albedo is a value which is interpolated between white-sky and black-sky albedo as a function of fractional diffuse skylight (which is a function of aerosol optical depth). NDVI was obtained from level 3 MODIS vegetation indices product (MYD13Q1, version 6.1), which are generated every 16-day at 250 meter (m) spatial resolution. All the input remote sensing variables mentioned in table 2 were resampled to spatial resolution of MYD11A2 product (923 m).

3.2 Sensitivity and statistical analysis

The accuracy of STIC-TI heavily depends on the accuracy of T_S, NDVI, and α_R due to the dual role of T_S in estimating M and G_i, the role of NDVI in G_i, and the combined role of T_S and α_R in estimating R_{Ni}. Therefore, one-dimensional sensitivity analysis was conducted to assess the impacts of uncertainty in T_S, NDVI and α_R on G_i, H_i and LE_i. The sensitivity was assessed by varying noon-time T_S by ±0.5 K, ±1.0 K and ±1.5 K (keeping nighttime T_S constant so that amplitude can vary automatically); varying NDVI by ±0.05; ±0.10, ±0.15; and varying albedo by ±0.02, ±0.05, ±0.10, respectively. SEB fluxes were computed by using T_S, NDVI, and α_R for three different periods of the year in all the eight ecosystems. Sensitivity analyses were conducted by increasing and decreasing systematically T_S, NDVI, α_R from its central value while keeping the other variables and parameters constant. This procedure was selected because the

fluxes and intermediate outputs of the STIC-TI model reflect an integrated effect due to uncertainty in T_S. In the first run, SEB fluxes were computed using *in-situ* T_S measurements obtained from the flux tower outgoing longwave radiation measurements. Then T_S was increased and decreased at constant interval and a new set of fluxes were estimated. In the similar way, α_R and NDVI were increased and decreased at constant intervals and new set of fluxes were computed. The sensitivity of STIC-TI was assessed by the equation 14.

$$\text{Sensitivity} = \frac{E_{i0} - E_{iM}}{O_i} * 100 \quad (14)$$

E_{i0} is the estimated (original) model output and E_{iM} is the estimated (modified) output obtained by changing the variable whose sensitivity is to be tested. O_i is actual measurements. Apart from the sensitivity analysis, the following set of statistical metrics were used to assess model performances.

$$R^2 = \left(\frac{\sum_{i=1}^{n}(E_i - \overline{E})\,(O_i - \overline{O})}{\sqrt{\sum_{i=1}^{n}(E_i - \overline{E})^2}\sqrt{\sum_{i=1}^{n}(O_i - \overline{O})^2}} \right)^2 \quad (15)$$

$$\text{RMSE} = \sqrt{\sum_{i=1}^{n} \frac{(E_i - O_i)^2}{n}} \quad (16)$$

$$\text{BIAS} = \frac{\sum_{i=1}^{n}(E_i - O_i)}{n} \quad (17)$$

$$\text{MAPD} = \frac{100}{n}\sum_{i=1}^{n}\left|\frac{E_i - O_i}{O_i}\right| \quad (18)$$

$$\text{KGE} = 1 - \sqrt{(r-1)^2 + \left(\frac{\sigma_E}{\sigma_o} - 1\right)^2 + \left(\frac{\overline{E}}{\overline{O}} - 1\right)^2} \quad (19)$$

Where R^2 is the coefficient of determination, RMSE is root-mean-square error, BIAS is the mean bias, MAPD is the mean absolute percent deviation, KGE is Kling-Gupta efficiency, n is the total number of data pairs, the bar indicates mean value of the measured variable and model estimates of the same variable. E_i and O_i are the model estimated and measured SEB fluxes, r is the Pearson's correlation coefficient and $\overline{O}$ is the average of measured values and $\overline{E}$ is the

average of estimated values and σ_o is standard deviation of observation values and σ_E is the standard deviation of estimated values. The KGE has been widely used for calibration and evaluation hydrological models in recent years and it combines the three components of Nash-Sutcliffe efficiency (NSE) of model errors (i.e., correlation, bias, ratio of variances or coefficients of variation) in a more balanced way. But it has not been widely used for analyzing the ET model performances. KGE = 1 indicates perfect agreement between modeled estimates and observations. The performance of a model is considered 'poor' for KGE between 0 and 0.5 and models with negative KGE values is considered 'not satisfactory'.

4 Results

4.1 Ecosystem- scale surface soil temperature amplitude (A)

The scaling functions developed to estimate ecosystem-scale (1km) surface soil temperature amplitude (A) from point-scale T_{STA} were used to estimate G_i. However, before the development of the scaling functions, analysis was carried out to investigate the relationship of soil temperature amplitude between the two different spatial scales. The scatterplot (Fig. 5a) of noon-night LST difference (ΔTs) versus T_{STA} for different albedo classes showed a linear increase in ΔTs with increasing T_{STA}. However, some divergence of data points within the cluster were also noticed which could be associated with different albedo (α_R) levels. Bivariate linear function was fitted between T_{STA} as predictand (Y) versus ΔTs ($T_{sd} - T_{sn}$) and α_R as predictors (X1 and X2, respectively). The function was found to be $Y = 0.59X1 - 51.3X2 + 8.66$ by combining the data of nine ecosystems ($r = 0.86$). The coefficients in the above expressions correspond to B1 (0.59), B2 (51.3), B3 (8.66) of eq. 5 in section 3.1.1.1. The estimated amplitude from this ecosystem-scale predictors and scaling functions was treated as ecosystem-scale surface soil temperature amplitude (A).

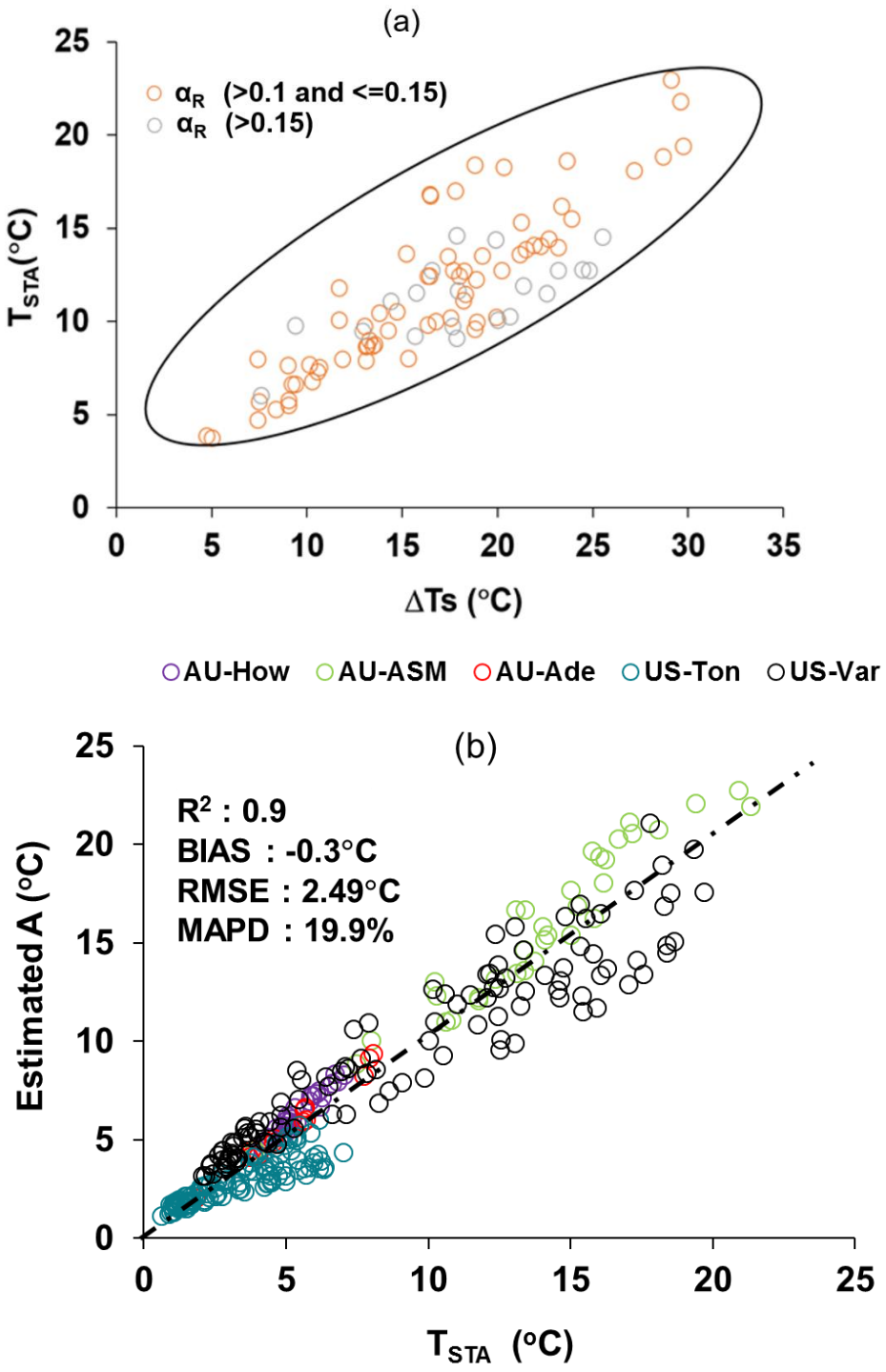

Figure 5. (a) Two-dimensional scatterplots between (ΔTs) versus T_{STA} at different α_R levels over different ecosystems. Here T_{STA} in y-axis is the observed soil temperature amplitude that is used to develop the scaling function and delta ΔTs is noon-night LST difference of MODIS AQUA; (b) Validation of ecosystem-scale estimates of A from the above functions over different sites.

Validation of ecosystem-scale estimates of A from the above functions over different sites is shown in Fig. 5b with respect to T_{STA} for the independent datasets. The estimated A was found to have MAPD of 19.9%, negative bias, and R^2 = 0.90 over different ecosystems. The temporal variation of estimated A and T_{STA} is shown in Fig D1 in Appendix D. Further analysis was carried out to investigate the bias in A at three fractional vegetation cover (fc) slabs (fc<0.3; 0.3≤fc≤0.5; fc>0.5) representing bare soil (slab 1), 30 – 50% canopy cover (slab 2) and more than 50% canopy cover (slab 3), respectively. While negative bias was noted for slab 1 and slab 3 (-0.54°C and -0.83° C), the bias was positive (0.49° C) in the intermediate fc which represents sparse and patchy canopy cover. The signals of surface albedo, emissivity and temperatures of soil surface and canopy are relatively pure in slab1 and slab 3 as compared to slab 2, where the surface signal carries more heterogeneity. Given T_{STA} is computed from the in-situ measurements, it is likely to carry more heterogeneity in slab 2 as compared to the other two slabs. The land surface emissivity in MYD11A2 was estimated from land cover types and anisotropy factor, which have differential impacts on T_{ST} and T_S leading to such opposite bias in slab 2 as compared to slab 1 and slab 3.

4.2 Sensitivity analysis of STIC-TI G_i, LE_i and H_i to land surface variables

4.2.1 Sensitivity of G_i to land surface variables

The average sensitivity of G_i to three land surface variables (T_S, NDVI, α_R) by combining the estimates of wet and dry periods is shown in Fig. 6. G_i was found to be substantially sensitive to T_S with error magnitude ranging from 2 – 18% due to T_S uncertainties of ±0.5 – 2.5 K (Fig. 6a), with greater sensitivity to T_S during the summer season as compared to other seasons. The median sensitivity of G_i due to ±5 – 10% uncertainty in α_R varied from 5 to 12% in all the ecosystems (Fig. 6b). The uncertainties in NDVI revealed 2 to 15% error in G_i estimates (Fig. 6c), and no significant difference in the mean sensitivity due to NDVI uncertainties was noted between the ecosystems. The sensitivity of G_i decreased with increasing values of NDVI.

4.2.2 Sensitivity of LE_i and H_i to land surface variables

Both LE_i and H_i were sensitive to T_S to the order of 2 – 29% (LE_i) and 5 – 35% (H_i) for T_S uncertainty of ±0.5 – 2.5 K from its mean values (Table 3). Interestingly, LE_i was more sensitive to T_S uncertainties as compared to H_i in the rainfed ecosystems. The highest mean sensitivity of

522 LE_i to T_S was found in arid (IND-Jai: 2 – 28%), semi-arid (AU-ASM: 5 – 21%), tropical savanna
523 (IND-Dha: 3 – 26%), savanna (US-Ton: 4-29%) and arid (US-Var: 3-26%) ecosystems. The
524 mean sensitivity of H_i to T_S was maximum in sub-humid (IND-Sam: 2 – 32%), semi-arid (IND-
525 Naw: 2 – 28%), savanna (AU-Ade: 8 – 17%) (Table 3). A greater sensitivity of the SEB fluxes
526 due to α_R uncertainties was found than due to NDVI. The median sensitivity of LE_i and H_i due to
527 10% uncertainty from mean α_R varied within 2 – 16% in all the ecosystems (Table 3). By
528 contrast, errors in the two SEB fluxes were substantially low (2 – 13%) due to ±0.05 – 0.15
529 uncertainty from mean NDVI (Table 3).

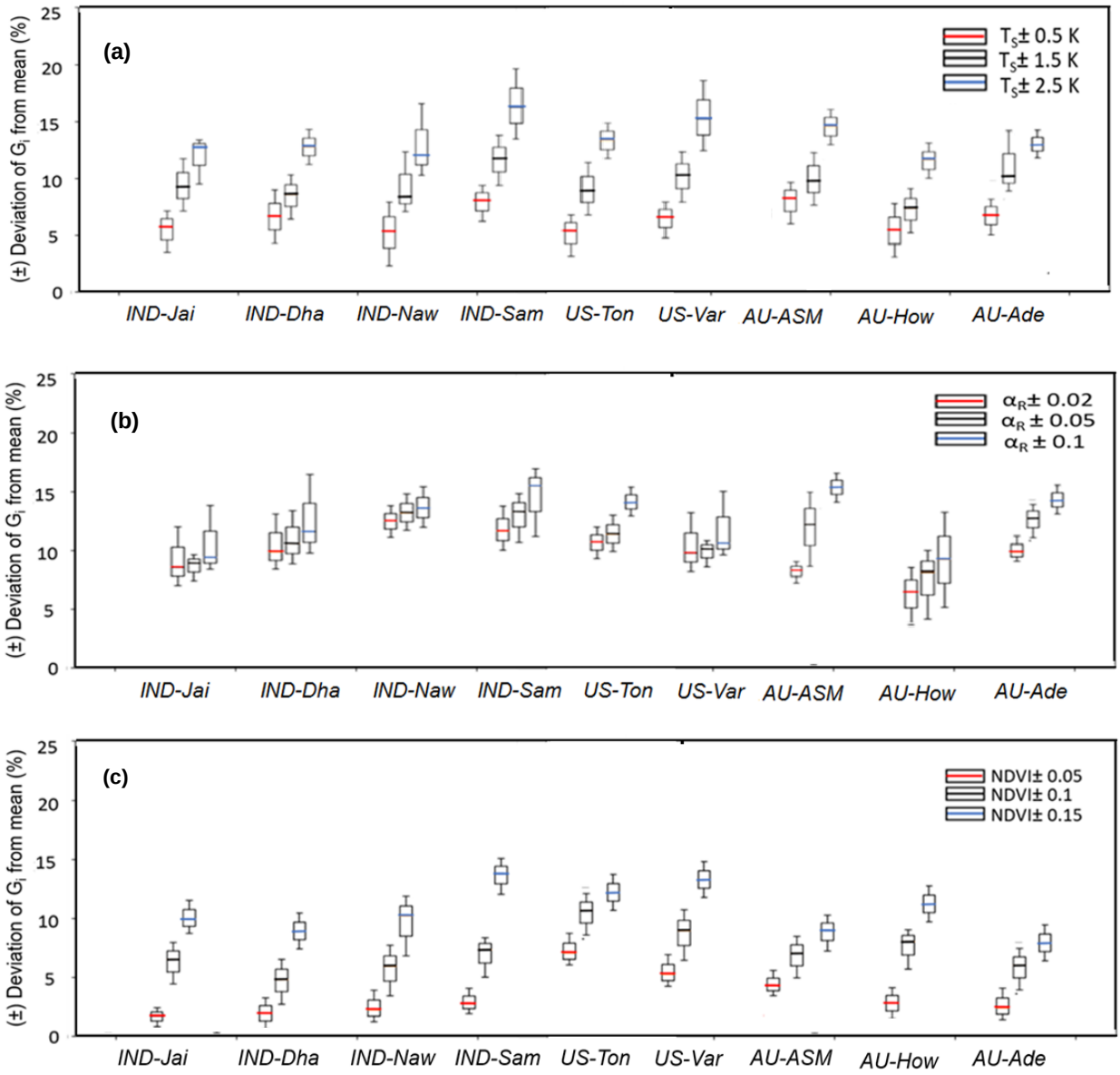

Figure 6: Sensitivity of STIC-TI G_i due to uncertainties in T_S (a), α_R (b), and NDVI (c) for eight

flux tower sites in India and Australia. The uncertainties were introduced by taking the mean values of these variables during three different periods (summer, rainy and winter) of a year. Mean uncertainties of the three periods are presented in the figure.

Table 3: Sensitivity (in percent) of LE_i and H_i due to T_S, NDVI, and α_R uncertainties

Study sites	Sensitivity of LE_i and H_i to T_S, NDVI and α_R (percent change)					
	T_S uncertainty (*±0.5 – 2.5 K*)		α_R uncertainty (*±5 – 10%)*		NDVI uncertainty (*±0.05 – 0.15)*	
	LE_i	H_i	LE_i	H_i	LE_i	H_i
IND-Jai	2-28	1-6	3-14	2-13	2-8	2-6
IND-Dha	3-26	2-8	2-12	3-12	3-10	3-9
IND-Naw	1-20	2-28	2-10	3-10	2-7	2-6
IND-Sam	1-16	5-32	4-13	6-11	2-5	2-7
US-Ton	4-29	4-12	3-12	4-12	3-8	5-7
US-Var	3-26	6-14	4-11	2-10	4-10	2-8
AU-ASM	5-21	2-10	3-12	2-13	2-10	2-11
AU-How	8-13	2-15	2-11	4-16	3-12	3-13
AU-Ade	2-17	8-17	3-12	2-10	3-10	3-9

4.3 Comparative evaluation of STIC-TI and contemporary G_i models

The performances of STIC-TI and existing G_i models were evaluated and compared with respect to *in-situ* G_i measurements. The existing models reported by Moran et al. (1989), Bastiaanssen et al. (1998), Su (2002), and Boegh et al. (2004) have been considered for comparing with TI-based model. These four existing models are referred here as MOR89, BAS98, SU02 and BO04, respectively. While the models MOR89, SU02 and BO04 are based on linear regression between G versus NDVI, BAS98 is based on multivariate regression of G with NDVI, LST and α_R. The performance of the STIC-TI was substantially better as compared to MOR89, SU02 and BO04 with respect to MAPD (19%), RMSE (22 Wm^{-2}) and coefficient of determination (R^2 = 0.8) when compared with *in-situ* measurements over one Indian, three Australian and two US flux

542 tower sites (Table 4) and also comparable with BAS98 G_i model. The validation plot of retrieved
543 noontime Gi from STIC-TI is shown in Fig. 7.

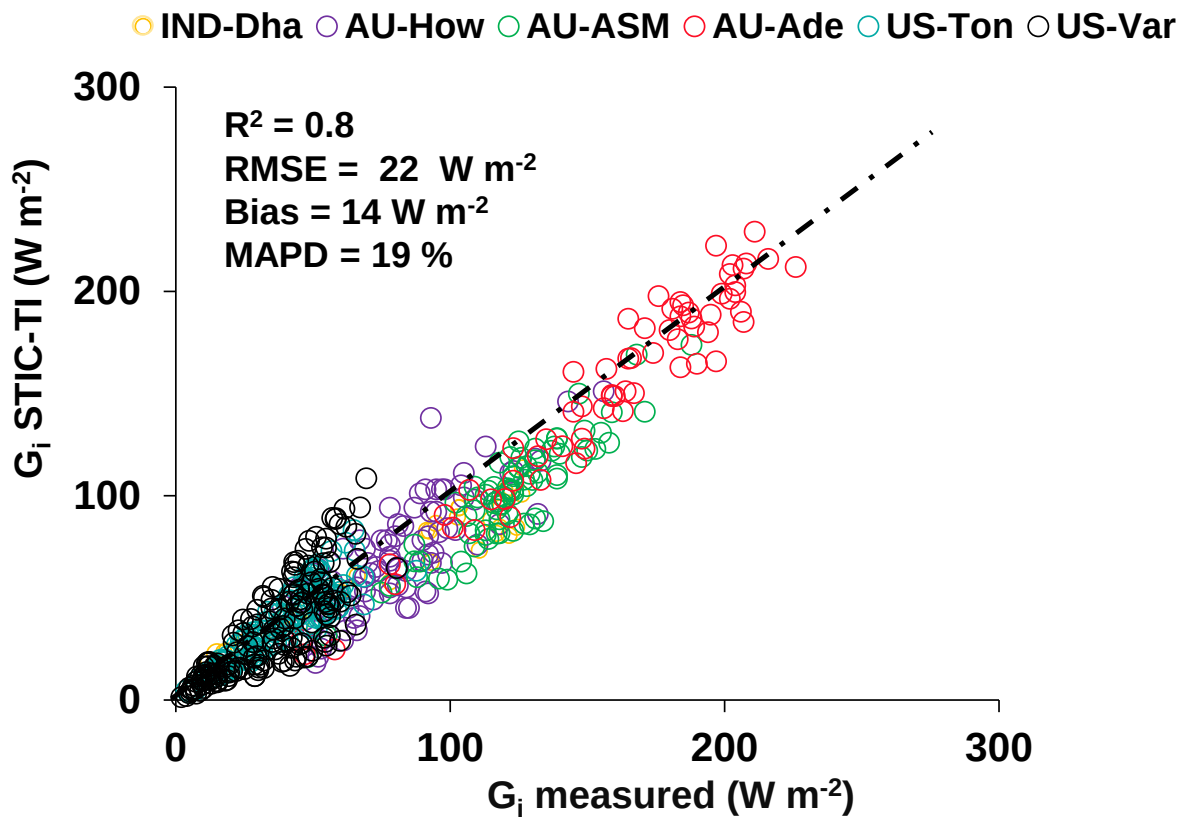

Figure 7: Validation of noontime (1:30 pm) G_i estimates with respect to in-situ measurements in different ecosystems. The regression between the two sources of G_i is G_i (STIC-TI) = 0.90G_i (tower) -0.10.

544 **Table 4**: A comparison of error statistics of G_i estimates from STIC-TI and existing G_i models
545 over different ecosystems

G models	R^2	RMSE (W m^{-2})	MAPD (%)	KGE
STIC-TI	0.80	22	19	0.74
MOR89	0.70	31	29	0.46
BAS98	0.80	20	18	0.61
SU02	0.80	30	26	0.54
BO04	0.70	35	29	0.48

546 The RMSE varied from 9 to 20 W m^{-2} with MAPD ranging from 12 to 21% across individual
547 flux tower sites. High magnitude of G_i was predicted in the arid and semi-arid systems (120 –

240 W m^{-2}) as compared to the humid systems (20 – 90 W m^{-2}), which was in close correspondence with the observations. The model also captured the range of G_i that are generally found in different biomes (20 – 140 W m^{-2} for grasslands, 20 – 90 W m^{-2} for cropland) (Purdy et al., 2016). Due to the paucity of G_i measurements, direct validation of G_i was only possible for 32 days (concurrent to MODIS overpass) at the IND-Dha site. Overall, STIC-TI tends to provide reasonable G estimates for the terrestrial ecosystems having soil temperature amplitude above 5ºC.

4.4 Evaluation of STIC-TI LE_i, H_i, and EF

The modeled versus measured LE_i and H_i showed good agreement in all the nine ecosystems with RMSE in LE_i and H_i estimates using MYD11 LST product to the order of 29 – 62 W m^{-2} and 26 – 61 W m^{-2}, MAPD of 9 – 31% and 20 – 36%, BIAS of -29 to 38 W m^{-2} and -44 to 32 W m^{-2} (Fig. 8a, b; Table 5) and high R^2 of 0.8.

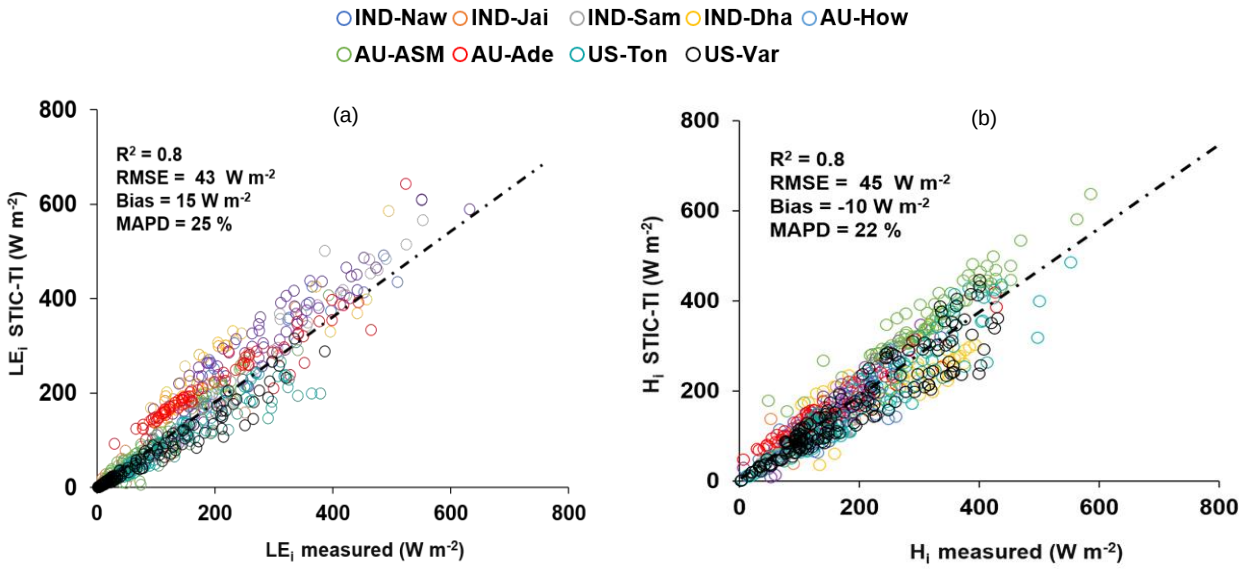

Figure 8: (a) Validation of STIC-TI LE_i estimates with respect to *in-situ* measurements in different ecosystems; (b) Validation of STIC-TI H_i estimates with respect to *in-situ* measurements in different ecosystems.

Table 5: Error statistics of STIC-TI LE_i and H_i estimates with respect to EC measurements in different ecosystems of India, US, and Australia using MYD11A2 LST product for all nine sites and using MYD21A2 LST product for three semi-arid and arid sites. The statistics obtained by using MYD21A2LST are shown in the parentheses.

Sites	STIC-TI (LE_i and H_i)									
	R2		BIAS (W m^{-2})		RMSE (W m^{-2})		MAPD (%)		KGE	
	LE_i	H_i	LE_i	H_i	LE_i	H_i	LE_i	H_i	LE_i	H_i
IND-Jai	0.90 (0.91)	0.90 (0.92)	-21 (-16)	12 (9)	57 (45)	27 (21)	31 (24)	22 (19)	0.80 (0.82)	0.76 (0.79)
IND-Naw	0.90 (0.92)	0.80 (0.85)	19 (12)	-26 (-16)	44 (37)	51 (46)	17 (16)	28 (25)	0.92 (0.92)	0.71 (0.73)
IND-Dha	0.90	0.90	38	-44	43	35	27	25	0.71	0.64
IND-Sam	0.90	0.80	12	-10	32	61	9	27	0.95	0.70
US-Ton	0.90 (0.91)	0.90 (0.92)	-29 (-18)	-32 (-21)	53 (45)	34 (27)	25 (22)	17 (15)	0.85 (0.87)	0.91 (0.93)
US-Var	0.90	0.80	-19	-28	49	39	27	20	0.82	0.89
AU-ASM	0.90 (0.93)	0.90 (0.91)	-3 (6)	22 (16)	46 (37)	26 (18)	29 (24)	20 (17)	0.94 (0.95)	0.83 (0.85)
AU-How	0.90	0.90	16	-25	42	27	17	21	0.89	0.85
AU-Ade	0.90	0.90	21	15	29	53	28	36	0.77	0.80

Arid ecosystems in India (IND-Jai), US (Ton and Var) and semi-arid ecosystem in Australia (AU-ASM) revealed relatively high MAPD (31%, 25%, 27%, and 28%) (Table 5). In general, STIC-TI was able to produce the dominant convective heat fluxes with respect to the EC measurements as evident through low RMSE for H_i and high RMSE for LE_i in the IND-Jai, US-Ton, US-Var, and AU-Ade where LE_i is inherently low except few rainy days. A uniform distribution of data points around 1:1 validation line (Fig. 8a) indicated overall low BIAS in LE_i estimates. However, modeled H_i was consistently lower than the observations (negative BIAS) in the tropical savanna (IND-Dha and AU-How) and semi-arid (IND-Naw) ecosystems [(-44) – (-25) W m^{-2} and -26 W m^{-2}) while a consistent positive BIAS was observed in the AU-ASM (semi-arid) and AU-Ade (savanna), US-Var (arid) (Fig. 8b; Table 5). This consequently led to overall low negative BIAS (-10 W m^{-2}), relatively low R^2 in H_i (R^2 = 0.8) as compared to the errors in LE_i (BIAS = 15 W m^{-2}, R^2 = 0.9). The regression between the modeled and tower measurements of LE_i is LE_i(STIC-TI) = 0.98LE_i(tower) – 0.266. The regression between the modeled and tower measurements of H_i is H_i (STIC-TI) = 0.93H_i(tower) + 4.90. The KGE statistics varied in the range of 0.71 – 0.95 for LE_i and in the range of 0.64 –0.91 for H_i, respectively across all nine flux tower sites, thus revealed reasonably high efficiency of the model to capture the magnitude and variability of SEB fluxes.

The effects of day-night view angle of MODIS Aqua on STIC-TI were further investigated, where the percent deviations in LE_i, H_i and G_i with respect to measurements were analysed in response to the day and night view angle distributed over 12 angular bins within ±50° at 10° interval. Number of occurrences of deviations in each bin of day view angle are plotted in Figure F (Refer Appendix F), which showed similar near normal distribution of the three fluxes with G_i deviation having less peak occurrence as compared to the other two. This is due to a smaller number of available datasets used in case of G_i. It has been found that 90% of deviations occur within -40° to 30°day view angle thus showing some impact of day view angle on the modeled fluxes. The night view angle variation apparently had no impact on the modelled fluxes.

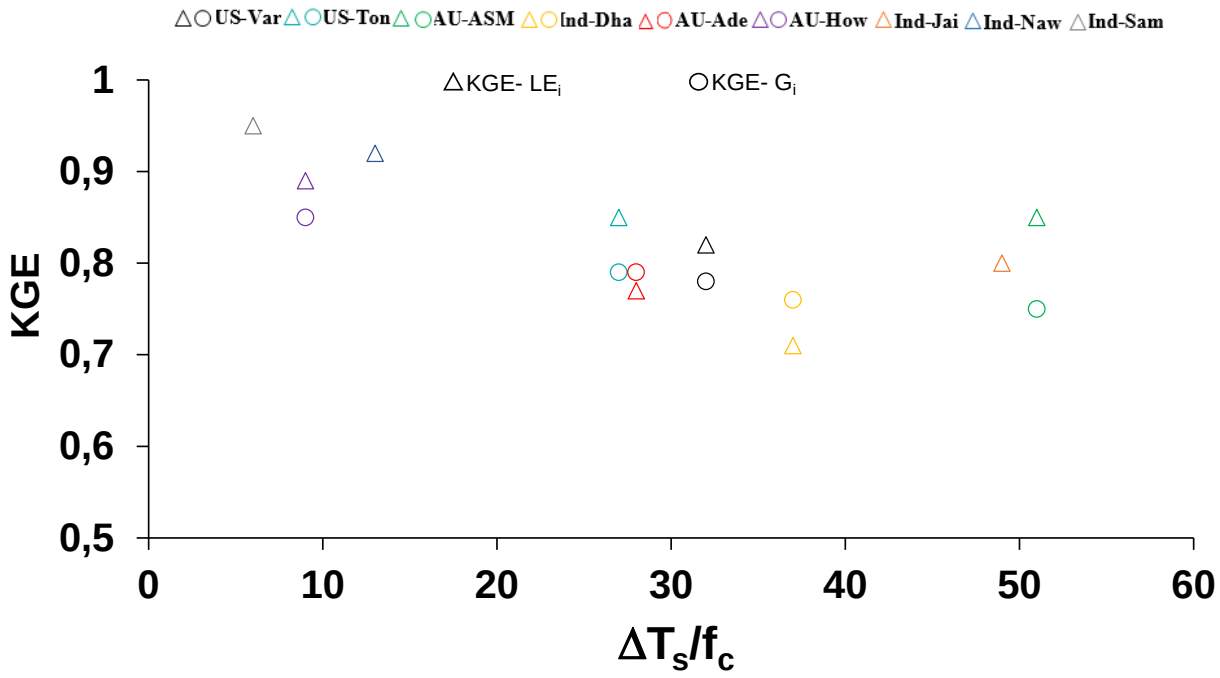

Figure 9: Relationship between KGE of STIC-TI (G_i and LE_i) with $\Delta T_s/f_c$ in different terrestrial ecosystems.

Further investigation was made on whether KGE for STIC-TI G_i and LE_i follow any systematic pattern and the ratio ΔT_S and f_c was used as proxy for surface heterogeneity and dryness. The plot of KGE of G_i and LE_i with this ratio is shown in Fig. 9. KGE-G_i was found to show a systematic decrease with increase in ΔTs-fc ratio up to 40, after which it remained unchanged with increase in the ratio. Although KGE of LE_i also decreased (20% reduction) with increase in ΔTs-fc ratio, KGE-LE_i was found to increase beyond ΔTs-fc 40. This revealed that the model

efficiency remained high (>0.8) within certain dryness limits (ΔTs-fc ratio <20 and >50) and the efficiency reduced moderately (within 0.7 – 0.8) for intermediate dryness. Interestingly, the use of MYD21A2 LST in STIC-TI showed improvements (see the parentheses in different columns in Table 5) in LE_i and H_i error statistics as compared to using MYD11A2 LST in terms of higher R^2 and KGE, and lower RMSE in LE_i (3-8% less) and H_i (2-3% less) for semi-arid and arid sites such as IND-Jai, IND-Naw and US-Ton.

An independent evaluation of multi-temporal heat fluxes over two US flux sites for the years 2016-2018 is shown in Fig. 10 and Fig 11. STIC-TI G_i estimates with MYD11A2 LST product showed close match with *in-situ* measurements with respect to intra and inter-annual variability in G_i followed by LE_i and H_i. This further demonstrates the merit of the coupled model for reproducing ecosystem-scale G_i estimates especially for shorter and open canopies.

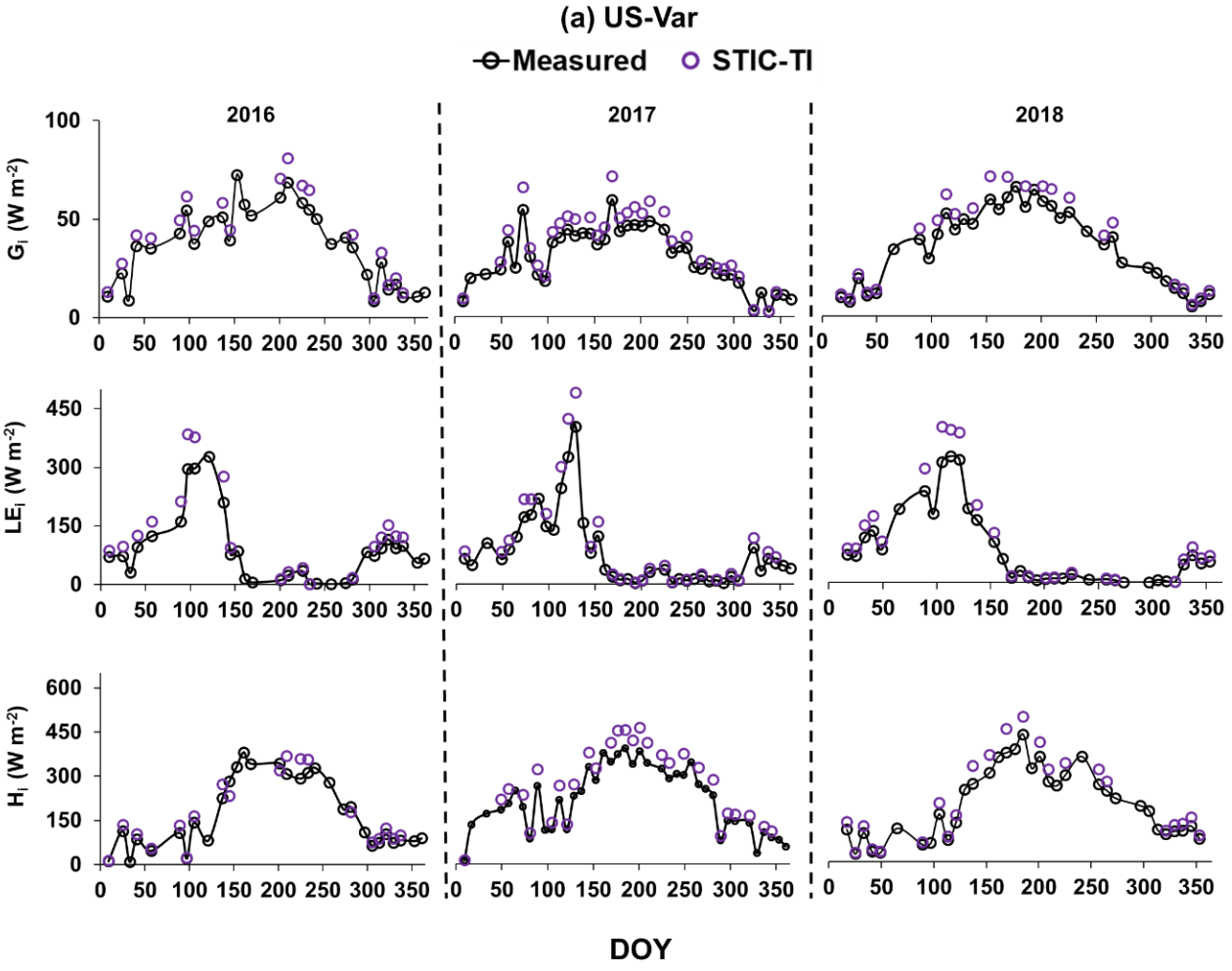

Figure 10: Illustrative examples of temporal evolution of STIC-TI derived fluxes using MYD11A2 LST product versus observed SEB fluxes for three consecutive years from 2016 to 2018 in a grassland ecosystem in United States (e.g., US-Var).

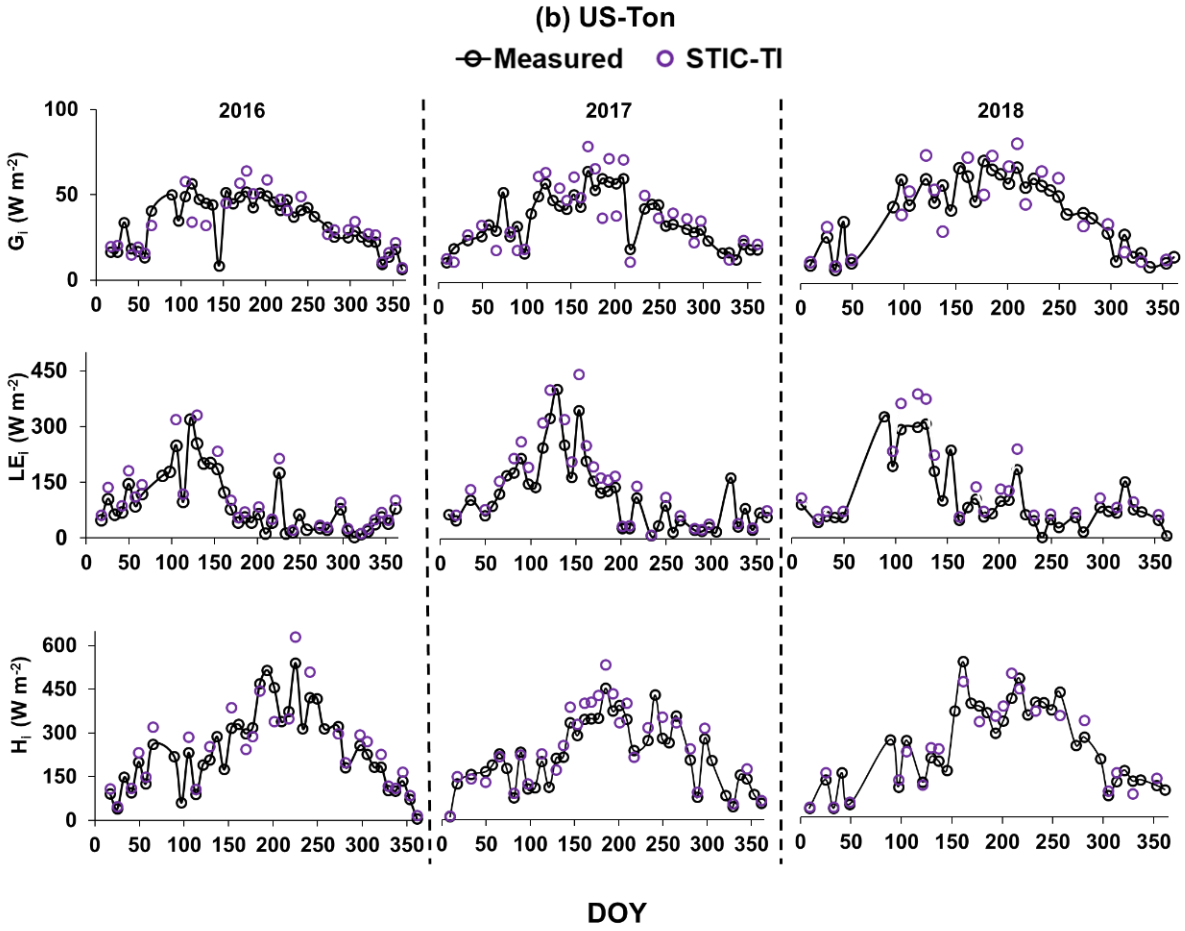

Figure 11: Illustrative examples of temporal evolution of STIC-TI derived fluxes using MYD11A2 LST product versus observed SEB fluxes for three consecutive years from 2016 to 2018 in a woody savanna ecosystem in the United States (e.g., US-Ton).

609 The temporal behavior of STIC-TI and observed evaporative fraction (EF) (ratio of LE and R_N –
610 G) (Fig. 12) along with observed monthly rainfall (P) distinctly captured the substantial temporal
611 variability in EF during the dry-to-wet transition in the Indian study sites, which also
612 corresponded to low (high) θ and P. In IND-Naw and IND-Sam, a marked rise (>0.4) in STIC-TI
613 EF was noted during day-of-the-year (DOY) 25 to 75 where wheat is grown under assured
614 irrigation. The impact of irrigation is thus captured by the substantial increase in EF in the
615 absence of P. In contrast, the rainfed grassland system (IND-Jai) showed peak EF (~0.8), which
616 corresponded to south-west monsoon rainfall during June to September and a progressive decline

in EF during the dry down period in October to April corresponding to post south-west monsoon phase. Some intermittent spikes in EF were also noted during dry-down phase in both STIC-TI and observations. The intermittent EF spikes during the soil moisture dry down phase could be due to enhanced LE through moisture advection from the surrounding vegetation causing an enhancement of evaporation than expected. This is known as the 'clothesline effect' which frequently occurs in semi-arid and arid ecosystems. In addition to IND-Jai, the response of both modeled and measured EF to wet and dry spells was also noted during south-west monsoon period at all other flux tower sites of India.

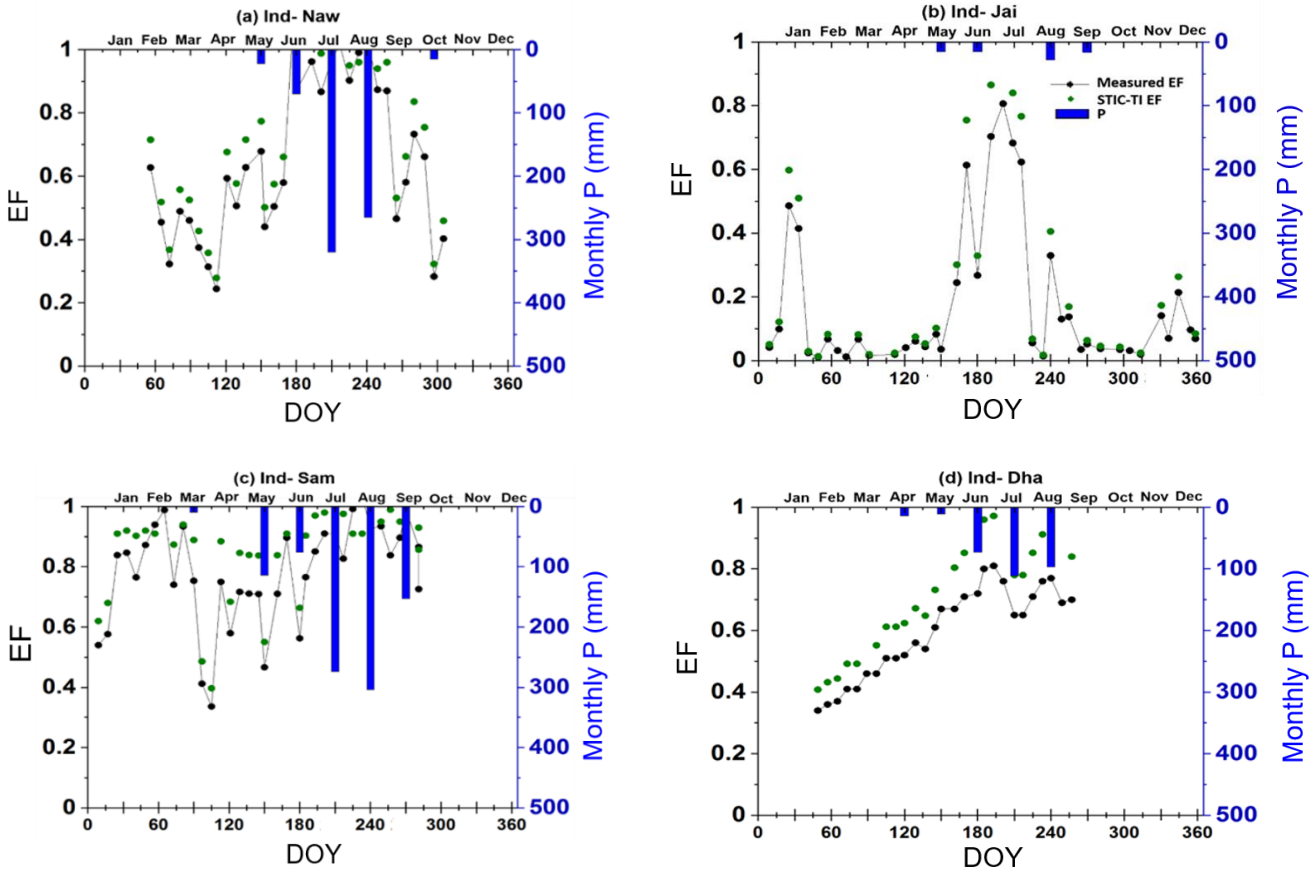

Figure 12: Illustrative examples of temporal variation of STIC-TI derived EF using MYD11A2 LST product with respect to measured EF and P in (a) IND-Naw, (b) IND-Jai, (c) IND-Sam, and (d) IND-Dha

The temporal behavior of EF from STIC-TI using MYD11A2 LST product and EC measurements along with measured θ and P at the OzFlux and AmeriFlux sites also revealed (Fig. 13) close correspondence of STIC-TI with EC observations. Low EF (0.05 – 0.40) during the dry season around DOY 100 – 250 and high EF (>0.4) during the wet season (DOY 1 – 120

and 300 to 360) in AU-ASM, US-Ton and US-Var was observed. The analysis showed that STIC-TI EF can capture the annual variability of observed EF and its responses across different ecosystems during wet and dry seasons. The plots of STIC-TI EF versus measured θ (in the inset of Fig. 13) revealed triangular scatter close to right-angled triangle with positive slope of hypotenuse in three ecosystems AU-ASM, US-Var and US-Ton. This showed that in the water-controlled ecosystems, where distinct wet-dry seasons exist, the positive EF-θ relationship is an outcome of the soil moisture controls on transpiration during the dry season.

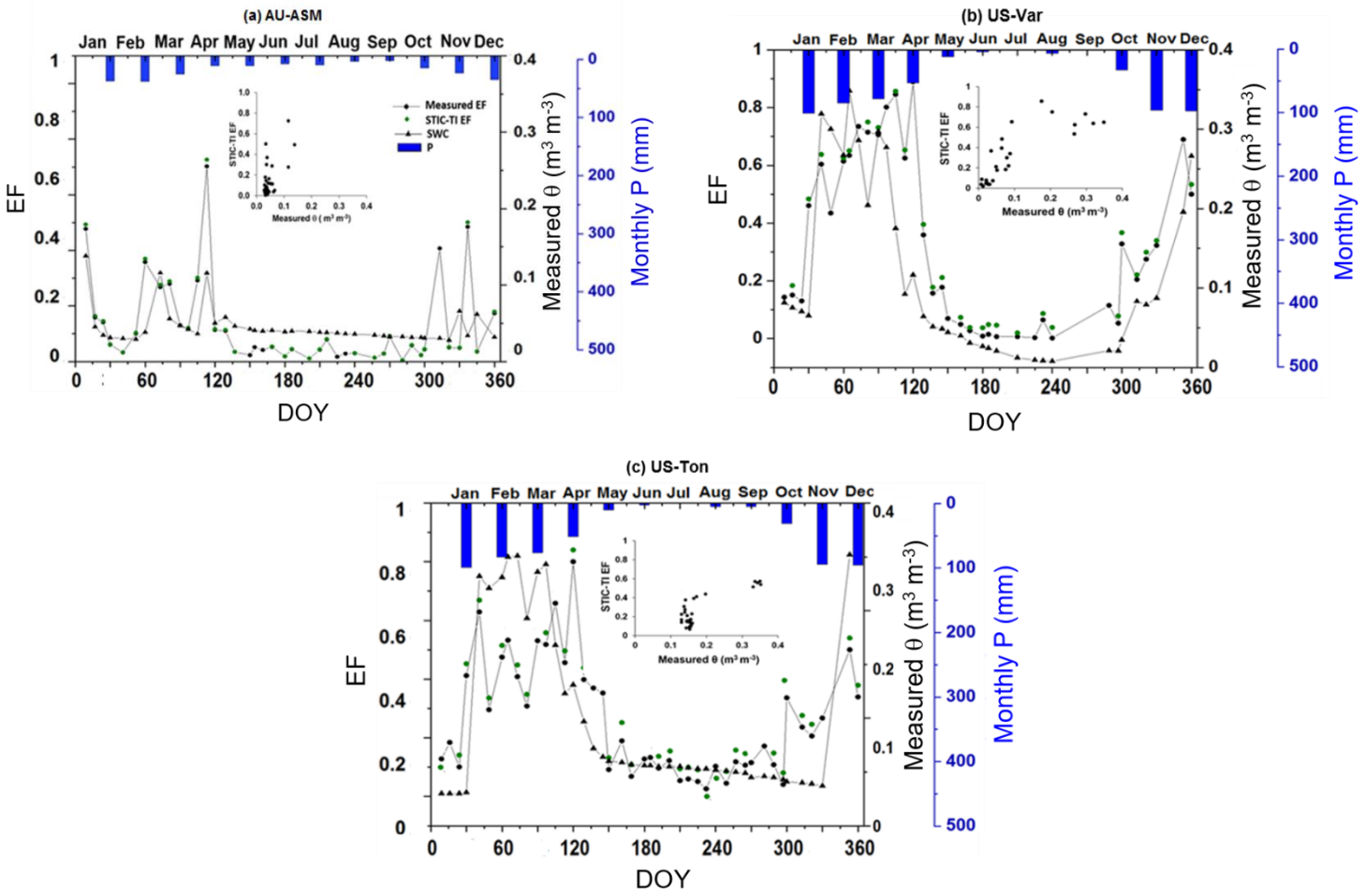

Figure 13: Comparison of temporal variation of STIC-TI derived EF using MYD11A2 LST with respect to measured EF, θ and Pin (a) AU-ASM, (b) US-Var, (c) US-Ton. The scatterplots in the inset shows the relationship between STIC-TI EF with respect to measured θ.

5 Discussion

5.1 Interaction of flux and internal SEB metrices

From section 4.1 we found relatively reduced sensitivity of G_i to Ts uncertainties. In any given condition, if an over(under) estimation of M due to noontime T_S uncertainties (through eq. 13) leads to an over(under) estimation of Γ, the effects of such over(under) estimation of Γ(due to noontime T_S uncertainties) tend to be compensated by under(over) estimation of amplitude A (in eq. 5), ultimately leading to a reduction of the sensitivity of G_i to T_S. While the scatter between G versus A for a wide range of Γ (Fig. 14a) revealed large scatter with increasing amplitude under the dry conditions (low Γ), the scatter between Γversus T_S for different M (Fig. 14b) revealed exponential reduction of Γ with increasing Ts and dryness, and almost no significant change in Γ with increasing T_S at a constantly high dryness (M<0.25). Thus, the confounding effects of Γ, A, and M through eq. 3, 5, 12 and 13 led to a reduction of sensitivity of G to T_S, as exemplified in Fig. 14.

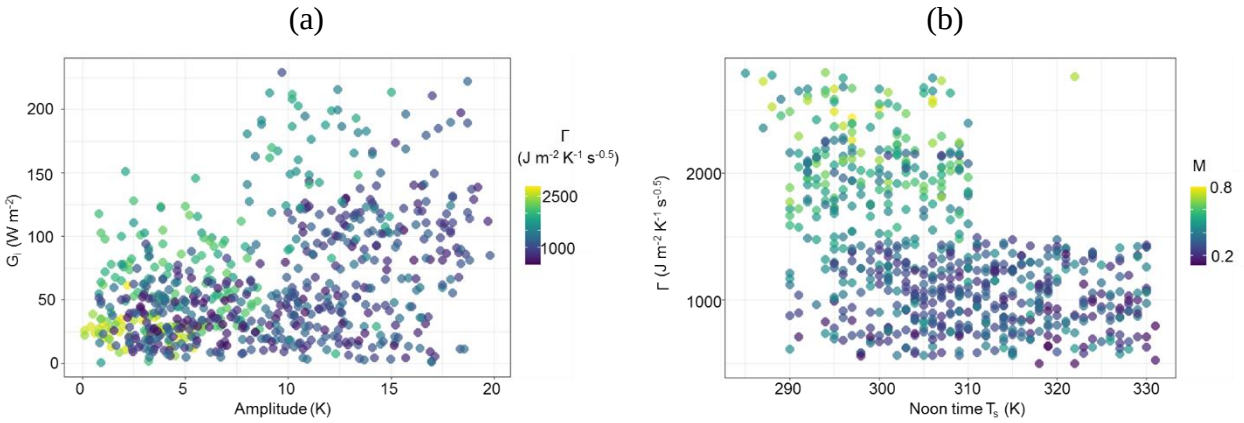

Figure 14: Response plots among parameters of TI-based G_i model, such as (a) G_i versus Amplitude (A) for varying Γ, and (b) Noon-time T_S versus Γ with varying M.

Concerning LE_i and H_i, dual uncertainties could be propagated in both the fluxes through daytime T_S (through M and G_i), leading to high sensitivity of these two SEB fluxes due to T_S perturbations. The relatively high sensitivity of LE_i to T_S (as compared to H_i) in the non-irrigated ecosystems could be due to partial compensation of g_A/g_S in both numerator and denominator of the PMEB equation for H (eq. C7 of Appendix C). A recent study (Fig.10 in Mallick et al., 2018a) showed high sensitivity of g_S due to T_S (1% change in T_S led to 5.2–7.5% change in g_S) as compared to g_A sensitivity to T_S (1% change in T_S led to 1.6–2%

change in g_A), suggesting that errors in g_S due to T_S uncertainty tend to be larger than errors in g_A. Partial cancellation of the conductance errors in the numerator of eq. (C7 of Appendix C) might have resulted in compensation of H_i errors in the water-limited ecosystems. In this environment, the variability of LE_i is mainly dominated by g_A/g_S, which makes LE_i highly sensitive due to T_S uncertainties. Combined uncertainty due to g_A/g_S in the denominator and g_A in the numerator of eq. (C6 of Appendix C) resulted into greater sensitivity in LE_i to T_S in the arid and tropical savannah ecosystems (Mallick et al., 2015, 2018a; Winter & Eltahir, 2010). The very low sensitivity of LE_i and Hi due to uncertainties in NDVI is because NDVI was not used in the conductance parameterizations and effects due to NDVI in STIC-TI was only propagated through G_i. The sensitivity of LE_i and H_i to albedo was mainly due to the dependence of net radiation (R_{Ni}) on albedo, and any resultant uncertainty in R_{Ni} (due to albedo) tends to be reflected in the sensitivity of LE_i and H_i to albedo.

5.2 Possible sources of errors in SEB flux evaluation

In STIC-TI, underestimation and overestimation errors in G_i in different ecosystems (Fig. 7) could originate due to the errors in MYD11A2 LST product. A host of studies previously reported that the standard deviations of errors in retrieved emissivity in bands 31 and 32 are 0.009, and the maximum error in retrieved Ts of MOD11A1 LST falls within 2-3 K, which is mainly due to the errors in surface emissivity correction (Duan et al., 2017; Wan, 2014; Lei et al., 2018). In the present analysis, we found an overestimation error of MODIS T_S in the range of 0.5 – 1.5 K when compared with *in-situ* infrared temperature measurements at the tropical savanna site. As mentioned in section 3.1, a positive (negative) bias in T_S would tend to an overestimation (underestimation) of amplitude (A) in eq. (5); underestimation (overestimation) of M in eq. (13), and consequent underestimation (overestimation) of Γ (eq. 12) and G_i, respectively. Furthermore, the standard deviation of NDVI surrounding the tower sites varied from 0.01 – 0.05 when compared to the ground measurements, which could be another source of error in the STIC-TI model. In addition, NDVI saturates at LAI > 3. However, STIC-TI provides direct estimates of ecosystem G and is independent of R_N.

Despite the comparable accuracy of current G estimates with the G model of Bastiaanssen et al (1998), the foundation of STIC-TI lies in the use of soil moisture characteristics with varying soil textural types which are known to influence the soil heat conductance and thereby G. Thus, the

687 control of soil moisture on evaporation is explicitly included in STIC-TI as opposed to the semi-
688 empirical G function of Bastiaanssen et al (1998). The higher accuracies of TI-based thermal
689 diffusion model as compared to R_N-based empirical G models were also reported by Purdy et al.
690 (2016) at daily or longer time scales in cropland, grassland. All these G model estimates many a
691 times differ from in situ measurements because of the no accounting of leaf litter presence or
692 layer on soil floor in the remote sensing-based G-model.
693 The overestimation (underestimation) of LE_i(H_i) is also due to the effects of spatial resolution of
694 different input variables on these two SEB fluxes and conducted statistical evaluation with
695 respect to the measured SEB fluxes. Eswar et al. (2017) demonstrated the need for spatial
696 disaggregation models for monitoring LE_i at field scale using contextual models by
697 disaggregation of evaporative fraction (Λ) and downwelling shortwave radiation ratio (R_G).
698 Using different disaggregation models, they estimated LE_i at 250m spatial resolution and
699 reported RMSE of 30 – 32 W m^{-2} as compared to LE_i obtained at 1000m spatial resolution with
700 RMSE of 40 – 70 Wm^{-2} over different sites in India. Anderson et al. (2007) reviewed different
701 validation experiments conducted in diverse agricultural landscapes (Anderson et al.,2004, 2005;
702 Norman et al., 2003) and reported RMSE in LE_i in the range of 35 – 40 W m^{-2} (15%) at 30 – 120
703 m disaggregated spatial resolution. Current analysis also brought out the need for noon-night
704 thermal imaging with spatial resolution finer than 1000m to adequately capture the magnitude
705 and variability of LE_i in the terrestrial ecosystems especially agroecosystems where average field
706 sizes are less (< 0.5 ha) and fragmented such as in India and other sub-continents.
707 As seen in Fig. 8a and Table 5, there is a gross overestimation of LE_i with respect to the tower
708 observations when MYD11A2 LST was used. The consistent positive BIAS in STIC-TI LE_i in
709 five out of nine sites is presumably due to the overestimation of R_{Ni} (Figure B1 of Appendix B)
710 and underestimation of G_i. Figure 7 shows overestimation of G_i for three OzFlux sites and US
711 sites and underestimation of G_i for Indian site with G_i (STIC-TI) = 0.90 G_i(tower) - 0.10 and
712 overestimation of R_{Ni} at the ecosystem-scale, with R_{Ni} (STIC-TI) = 0.78R_{Ni} (tower) +58.92
713 (Appendix-B2). This means a systematic overestimation of the net available energy (R_{Ni} – G_i)
714 will be obvious in cases where STIC-TI shows underestimation of G_i, which consequently leads
715 to an overestimation of retrieved LE_i. It may be also noted that the use of MYD21A2 LST led to
716 relatively better accuracy in LE_i (3-8%) and H_i (2-3%) as compared to using MYD11A2 LST in
717 semi-arid and arid ecosystems. The higher retrieval accuracy of MYD21A2 LST using TES

(Temperature-Emissivity Separation) algorithm over MYD11A2 LST that uses split-window algorithm (Wan et al, 2015) is the main reason for obtaining higher accuracy in LE_i and H_i estimates.

5.3 Effects of SEB closure

Given there is a widespread lack of SEB closure ($H + LE \neq R_N - G$) or residual energy balance, knowledge of the impact of different vegetation types and climatic variables on SEB 'non-closure' is essential. A recent study by Dare-Idowu et al. (2021) covering 8 growing seasons and 3 crops (maize, wheat, and rapeseed) in two sites of south-western France showed that the systematic effect of each site on SEB closure was stronger than the influence of crop type and stage. Same study revealed a greater percentage of SEB closure under unstable atmospheric conditions and in the prevailing wind directions, and sensible heat advection accounted for more than half of the imbalance at both the sites.

In our study, using unclosed SEB observations for Indian sites in the absence of *in-situ* G_i observations also added to the consistent positive BIAS in the statistical evaluation of LE_i. A ubiquitous lack of energy balance closure to the order of 10 – 20% worldwide at most of the EC sites is reported in different literatures (Stoy et al., 2013; Wilson et al., 2002), which implies a systematic underestimation (overestimation) of LE_i (EC tower) (and/or H_i(EC tower)). Accommodating an average 15% imbalance in LE_i (EC tower) would tend to diminish the positive BIAS in STIC-TI. Therefore, the pooled gain (0.98) and positive BIAS between the STIC-TI and tower LE_i is determined by the overestimation of ($R_{Ni} - G_i$), combined with the underestimation of measured LE_i from the EC towers. An underestimation of H_i (negative BIAS) is associated with two reasons; (a) ignoring the two-sided aerodynamic conductance of the leaves (Jarvis and McNaughton, 1986; Monteith and Unsworth, 2013; Schymanski et al., 2017), which could lead to substantial underestimation of H_i, and (b) due to the complementary nature of the PMEB equation, if LE_i is overestimated, H_i will be underestimated. In addition, frequent micro-advection fluxes alter measured in situ H and LE fluxes. But these advection conditions are not explicitly accounted in the current STIC-TI model. At the EC tower sites, the fraction of residual energy balance to R_N can be quantified with respect to vegetation/crop growth characteristics or biophysical properties. However, where G observations are lacking such as in many Indian EC

747 tower sites, the TI-based G model can be used to fill up the missing G observations to quantify
748 residual energy balance and to correct the SEB non-closure.

749 **6 Summary and conclusions**

750 This study addressed one of the outstanding challenges in simultaneous retrieval of ground heat
751 flux (G) and evaporation (ET) in open canopy, water-controlled and radiation-controlled
752 ecosystems. It demonstrated coupling of a thermal inertia (TI)-based mechanistic G model with a
753 surface energy balance (SEB) model (Surface Temperature Initiated Closure, STIC) using
754 satellite-based land surface temperature (Ts) and associated biophysical variables and has
755 minimal independence on *in-situ* measurements. The model is called STIC-TI, and this is the
756 first ever implementation of a coupled G-SEB model which also does not require any empirical
757 function for inferring the aerodynamic (g_A) and canopy-surface (g_S) conductance. The estimation
758 of g_A and g_S in STIC-TI is independent of any parameterization of surface roughness and
759 atmospheric stability and does not involve any look-up table for biome or plant functional
760 attributes. By linking T_S with thermal inertia (Γ) and surface moisture availability (M), STIC-TI
761 derives G through the harmonics equation between G and Γ, and subsequently coupled G with
762 the SEB fluxes. Independent validation of STIC-TI using measured flux data from nine terrestrial
763 ecosystems in arid, semi-arid and sub-humid climate in India, USA (representing northern
764 hemisphere) and Australia (representing southern hemisphere) led us to the following
765 conclusions:

766 (i) The retrieved G and associated SEB fluxes through STIC-TI were reasonably sensitive to
767 uncertainties in T_S and vegetation index. However, a compensation effect was evident due to
768 the partial cancellation of overestimated TI and underestimated A in the harmonics equation
769 of G. Both, latent and sensible heat fluxes (LE and H), were extremely sensitive to T_S
770 uncertainties, with maximum sensitivity of LE (H) to T_S found in arid and semi-arid (sub-
771 humid) ecosystems.
772 (ii) G estimates through STIC-TI performed better as compared to most of the contemporary
773 empirical G models, with lower MAPD and higher correlation coefficient with respect to *in-*
774 *situ* measurements. The most notable advantages of STIC-TI are, (a) it provides direct
775 estimates of G and is not dependent on net radiation estimates, (b) the ecosystem-scale

surface soil temperature amplitude used in G model can advance our understanding on associated terrestrial ecosystem processes.

(iii) Underestimation of G in some ecosystems was primarily attributed to the inherent bias in MODIS T_S product, NDVI saturation at higher LAI (>3) in conjunction with the spatial scale mismatch between single MODIS pixel and the footprint of G measurements. The consequent overestimation (underestimation) of LE (H) in some ecosystems was associated with the overestimation of net available energy, use of 'unclosed' SEB observation in LE and H validation, the spatial scale discrepancy between MODIS pixel versus eddy covariance measurement footprint, the complementary nature of the Penman Monteith Energy Balance equation (for H), and possibly due to ignoring the two-sided aerodynamic conductance by the leaves (for H), respectively.

(iv) While the MODIS Aqua day view angle within -40° to 30°showed moderate impact on the deviations in the modeled heat fluxes, the night view angle had no impact on the flux deviations.

The requirement of few input variables in STIC-TI generates promise for surface-atmosphere exchange studies using readily available data from the current generation remote sensing satellites (e.g., MODIS, INSAT) that have noon-night TIR observations. STIC-TI can be potentially used for distributed ET mapping using current and future 4th generation Indian Geostationary satellite observations from INSAT as well as future high spatial resolution (~ 60m) TIR observations with 3-day revisit from polar orbiting platform (Lagouarde et al., 2018, 2019) through the planned Indo-French space-borne mission, TRISHNA (**T**hermal infrared **I**maging **S**atellite for **H**igh-resolution **N**atural Resource **A**ssessment). This simple approach will also help in catering the need for a reliable, space-time continuous ET datasets in data-poor regions like Indian sub-tropics, South-East Asia, and other parts of the world from thermal remote sensing observation.

Author contributions

KM and BKB conceptualized the idea; DD conducted STIC-TI model coding, simulations and data analysis in consultation with KM and BKB; DD and BKB wrote the first version of the manuscript with KM writing the introduction, discussions and conclusions; all authors

contributed to discussions, editing and corrections; BKB and KM jointly finalized the manuscript.

Acknowledgement

The authors gratefully acknowledge Ministry of Earth Sciences (MoES), Govt. of India and National Environmental Research Council for providing necessary support through Indo-UK INCOMPASS programme (NE/L013819/1, NE/L013843/1, NE/L01386X/1, NE/P003117/1). BKB acknowledges Deputy Director, EPSA, SAC-ISRO and Director, SAC–ISRO for providing necessary support to participate and contribute to Indo-UK INCOMPASS programme. DD acknowledges Prof. P.D. Lele and Head from Department of Physics, Electronics and Space Sciences, Gujarat University Ahmedabad and for providing the necessary support to carry out this work. KM was supported through the International Mobility fellowship of Luxembourg National Research Fund (FNR) (INTER/MOBILITY/2020/14521920/MONASTIC). KCN is supported by the Jet Propulsion Laboratory, California Institute of Technology, under contract with the National Aeronautics and Space Administration and Government sponsorship is acknowledged. DDB acknowledges support from NASA Ecostress project and the US Department of Energy, Office of Science which supports the AmeriFlux project

Data and code availability

Harmonized time series datasets over the study grids are available in https://doi.org/10.5281/zenodo.5806501. The model code is available to the first author upon reasonable request.

References

Anderson, M., Kustas, W., Alfieri, J., Gao, F., Hain, C., Prueger, J., Evett, S., Colaizzi, P., Howell, T. and Chávez, J.: Mapping daily evapotranspiration at Landsat spatial scales during the BEAREX’08 field campaign, Adv. Water Resour., 50, 162 – 177, https://doi.org/10.1016/j.advwatres.2012.06.005, 2012.

Anderson, M., Norman, J., Kustas, W., Li, F., Prueger, J. and Mecikalski, J.: Effects of Vegetation Clumping on Two–Source Model Estimates of Surface Energy Fluxes from an

Agricultural Landscape during SMACEX, J. Hydrometeorol., 6(6), 892 – 909, https://doi.org/10.1175/JHM465.1, 2005.

Anderson, M., Norman, J., Mecikalski, J., Otkin, J. and Kustas, W.: A climatological study of evapotranspiration and moisture stress across the continental United States based on thermal remote sensing: 1. Model formulation, J. Geophys. Res.: Atmos., 112(D10), https://doi.org/10.1029/2006JD007506, 2007.

Anderson, M., Norman, J., Mecikalski, J., Torn, R., Kustas, W. and Basara, J.: A Multiscale Remote Sensing Model for Disaggregating Regional Fluxes to Micrometeorological Scales, J. Hydrometeorol., 5(2), 343 – 363, https://doi.org/10.1175/1525-7541(2004)005<0343:AMRSMF>2.0.CO;2, 2004.

Bai, Y., Zhang, S., Bhattarai, N., Mallick, K., Liu, Q., Tang, L., Im, J., Guo, L., and Zhang, J: On the use of machine learning based ensemble approaches to improve evapotranspiration estimates from croplands across a wide environmental gradient, Agric. Forest Meteorol., 298 - 299, 108308, https://doi.org/10.1016/j.agrformet.2020.108308, 2021.

Bastiaanssen, W. G. M., Menenti, M., Feddes, R. A. and Holtslag, A. A. M.: A remote sensing surface energy balance algorithm for land (SEBAL). 1. Formulation, J. Hydrol., 198-212, doi:10.1016/S0022-1694(98)00253-4,1998.

Bennett, W., Wang, J. and Bras, R.: Estimation of Global Ground Heat Flux, J. Hydrometeorol., 9(4), 744 – 759, https://doi.org/10.1175/2008JHM940.1, 2008.

Beringer, J., Hutley, L. B., McHugh, I., Arndt, S. K., Campbell, D., Cleugh, H. A., Cleverly, J., Resco de Dios, V., Eamus, D., Evans, B., Ewenz, C., Grace, P., Griebel, A., Haverd, V., Hinko-Najera, N., Huete, A., Isaac, P., Kanniah, K., Leuning, R., Liddell, M. J., Macfarlane, C., Meyer, W., Moore, C., Pendall, E., Phillips, A., Phillips, R. L., Prober, S. M., Restrepo-Coupe, N., Rutledge, S., Schroder, I., Silberstein, R., Southall, P., Yee, M. S., Tapper, N. J., van Gorsel, E., Vote, C., Walker, J., and Wardlaw, T.: An introduction to the Australian and New Zealand flux tower network – OzFlux, Biogeosciences, 13, 5895–5916, doi:10.5194/bg-13-5895-2016, 2016.

Bhat, G., Morrison, R., Taylor, C., Bhattacharya, B., Paleri, S., Desai, D., Evans, J., Pattnaik, S., Sekhar, M., Nigam, R., Sattar, A., Angadi, S., Kancha, D., Patidar, A., Tripathi, S., Krishnan, K. and Sisodiya, A.: Spatial and temporal variability in energy and water vapor

862 fluxes observed at seven sites on the Indian subcontinent during 2017, Q. J. R. Meteorolog.
863 Soc., 146 (731), https://doi.org/10.1002/qj.3688, 2853-2866, 2019.
864 Bhattarai, N., Mallick, K., Brunsell, N. A., Sun, G., and Jain, M.: Regional evapotranspiration
865 from an image-based implementation of the Surface Temperature Initiated Closure
866 (STIC1.2) model and its validation across an aridity gradient in the conterminous US,
867 Hydrol. Earth Syst. Sci., 22, 2311–2341, https://doi.org/10.5194/hess-22-2311-2018, 2018.
868 Bhattarai, N., Mallick, K., Stuart, J., Vishwakarma, B., Niraula, R., Sen, S. and Jain, M.: An
869 automated multi-model evapotranspiration mapping framework using remotely sensed and
870 reanalysis data, Remote Sens. Environ., 229, 69 – 92,
871 https://doi.org/10.1016/j.rse.2019.04.026, 2019.
872 Boegh, E., Soegaard, H., Christensen, J. H., Hasager, C. B., Jensen, N.O. and Nielsen, N. W.:
873 Combining weather prediction and remote sensing data for the calculation of
874 evapotranspiration rates: application to Denmark, Int. J. Remote Sens.,25, 2553 - 2574,
875 https://doi.org/10.1080/01431160310001647984, 2004.
876 Cammalleri, C. and Vogt, J.: On the Role of Land Surface Temperature as Proxy of Soil
877 Moisture Status for Drought Monitoring in Europe, Remote Sens., 7(12), 16849-16864,
878 https://doi.org/10.3390/rs71215857, 2015.
879 Cano, D., Monget, J., Albuisson, M., Guillard, H., Regas, N. and Wald, L.: A method for the
880 determination of the global solar radiation from meteorological satellite data. Solar Energy,
881 37(1), 840, 31 – 39, https://doi.org/10.1016/0038-092X(86)90104-0, 1986.
882 Castelli, F., Entekhabi, D. and Caporali, E.: Estimation of surface heat flux and an index of soil
883 moisture using adjoint-state surface energy balance, Water Resour. Res., 35(10), 3115 –
884 3125, https://doi.org/10.1029/1999WR900140, 1999.
885 Dare-Idowu, O., Brut, A., Cuxart, J., Tallec, T., Rivalland, V., Zawilski, B., Ceschia, E. and
886 Jarlan, L.: Surface energy balance and flux partitioning of annual crops in south-western
887 France. Agric. For. Meteorol., 308 – 309, 108529,
888 https://doi.org/10.1016/j.agrformet.2021.108529, 2021.
889 Didan, K.: MOD13Q1 MODIS/Terra Vegetation Indices 16-Day L3 Global 250m SIN Grid
890 V006., distributed by NASA EOSDIS Land Processes DAAC,
891 doi:10.5067/MODIS/MOD13Q1.006, 2021-06-06, 2015.

892 Donohue, R. J., Hume, I. H., Roderick, M. L., McVicar, T. R., Beringer, J., Hutley, L. B., Arndt,
893 S. K.: Evaluation of the remote-sensing-based DIFFUSE model for estimating
894 photosynthesis of vegetation, Remote Sens. Environ, 155, 349–365,
895 doi:10.1016/j.rse.2014.09.007, 2014.
896 Duan, A., Wang, M., Lei, Y. and Cui, Y.: Trends in summer rainfall over China associated with
897 the Tibetan Plateau sensible heat source during 1980–2008, J. Clim., 26, 261–275,
898 https://doi.org/10.1175/JCLI-D-11-00669.1, 2013.
899 Duan, S., Li, Z., Cheng, J. and Leng, P.: Cross-satellite comparison of operational land surface
900 temperature products derived from MODIS and ASTER data over bare soil surfaces. ISPRS
901 J. Photogramm. Remote Sens., 126, 1-10, https://doi.org/10.1016/j.isprsjprs.2017.02.003,
902 2017.
903 Eswar, R., Sekhar, M., Bhattacharya, B. and Bandyopadhyay, S.: Spatial Disaggregation of
904 Latent Heat Flux Using Contextual Models over India, Remote Sens., 9(9), 949,
905 https://doi.org/10.3390/rs9090949, 2017.
906 Friedl, M., McIver, D., Hodges, J., Zhang, X., Muchoney, D., Strahler, A., Woodcock, C.,
907 Gopal, S., Schneider, A., Cooper, A., Baccini, A., Gao, F. and Schaaf, C.: Global land cover
908 mapping from MODIS: algorithms and early results, Remote Sens. Environ., 83(1-2), 287 –
909 302, https://doi.org/10.1016/S0034-4257(02)00078-0, 2002.
910 Gao, Z., Horton, R. andLiu, H. P.:Impact of wave phase difference between soil surface heat
911 flux and soil surface temperature on soil surface energy balance closure, J. Geophys. Res.,
912 115, D16112, doi:10.1029/2009JD013278, 2010.
913 Hillel, D.: Introduction to Soil Physics, San Diego, US, ISBN 9780123485205, 1982.
914 Hulley, G., Malakar, N., and Freepartner, R.: Moderate Resolution Imaging Spectroradiometer
915 (MODIS) Land Surface Temperature and Emissivity Product (MxD21) Algorithm
916 Theoretical Basis Document Collection-6. Pasadena, California: Jet Propulsion Laboratory,
917 California Institute of Technology, 2016
918 Isaac, P., Cleverly, J., McHugh, I., van Gorsel, E., Ewenz, C., and Beringer, J.: OzFlux data:
919 network integration from collection to curation, Biogeosciences, 14, 2903–2928,
920 doi:10.5194/bg-14-2903-2017, 2017.
921 Jarvis, P.G. and McNaughton, K.G.: Stomatal Control of Transpiration – Scaling up from Leaf
922 to Region, Adv. Ecol. Res., 15, 1-49, https://doi.org/10.1016/S0065-2504(08)60119-1, 1986.

Johansen, O.: Thermal conductivity of soils, PhD Thesis, University of Trondheim. Hanover, NH: Cold Regions Research and Engineering Laboratory, US Army Corps of Engineers, CRREL Draft English translation, https://apps.dtic.mil/sti/pdfs/ADA044002.pdf, 1975.

Johnston, M., Andreu, A., Verfaillie, J., Baldocchi, D., and Moorcroft, P.: What lies beneath: Vertical temperature heterogeneity in a Mediterranean woodland savanna, Remote Sens. Environ., https://doi.org/10.1016/j.rse.2022.112950, 2022.

Kiptala, J., Mohamed, Y., Mul, M. and Van der Zaag, P.: Mapping evapotranspiration trends using MODIS and SEBAL model in a data scarce and heterogeneous landscape in Eastern Africa, Water Resour. Res., 49(12),8495 – 8510, https://doi.org/10.1002/2013WR014240, 2013.

Kustas, W. and Anderson, M.: Advances in thermal infrared remote sensing for land surface modeling, Agric. For. Meteorol., 149(12), 2071 – 2081, https://doi.org/10.1016/j.agrformet.2009.05.016, 2009.

Lagouarde J.-P., Bhattacharya BK, Crébassol P., Gamet P., Babu SS, Boulet G., Briottet X., Buddhiraju KM, Cherchali S., Dadou I., Dedieu G., Gouhier M., Hagolle O Irvine M., Jacob F., Kumar A., Kumar KK, Laignel B., Mallick K., Murthy CS, Olioso A., Ottle C., Pandya MR, Raju PV, Roujean J.-L., Sekhar M., Shukla MV, Singh SK, Sobrino J., Ramakrishnan R.: The Indian-French Trishna Mission: Earth Observation in the Thermal Infrared with High Spatio-Temporal Resolution, IGARSS 2018 - 2018 IEEE International Geoscience and Remote Sensing Symposium, Institute of Electrical and Electronics Engineers (IEEE). USA, 4078-4081, doi:10.1109/IGARSS.2018.8518720, 2018.

Lagouarde, J., Bhattacharya, B., Crébassol, P., Gamet, P., Adlakha, D., Murthy, C., Singh, S., Mishra, M., Nigam, R., Raju, P., Babu, S., Shukla, M., Pandya, M., Boulet, G., Briottet, X., Dadou, I., Dedieu, G., Gouhier, M., Hagolle, O., Irvine, M., Jacob, F., Kumar, K., Laignel, B., Maisongrande, P., Mallick, K., Olioso, A., Ottlé, C., Roujean, J., Sobrino, J., Ramakrishnan, R., Sekhar, M. and Sarkar, S.: Indo-French high-resolution thermal infrared space mission for earth natural resources assessment and monitoring – concept and definition of TRISHNA, ISPRS - International Archives of the Photogrammetry, Remote Sensing and Spatial Information Sciences, XLII-3/W6, 403-407, 2019.

Lu, L., Zhang, T., Wang, T. and Zhou, X.: Evaluation of Collection-6 MODIS Land Surface Temperature Product Using Multi-Year Ground Measurements in an Arid Area of Northwest China, Remote Sens., 10(11),1852, https://doi.org/10.3390/rs10111852, 2018.

Mallick, K.,& Bhattacharya, B.K., Chaurasia, S., Dutta, S., Nigam, R., Mukherjee J., Banerjee, S., Kar, G., Rao, V.,Gadgil, A.., Parihar, J.: Evapotranspiration using MODIS data and limited ground observations over selected agroecosystems in India, Int. J. Remote Sens., 28(10), 2091-2110, https://doi.org/10.1080/01431160600935620, 2007.

Mallick, K., Bhattacharya, B. K., Rao, V. U. M., Reddy, D.R., Banerjee, S., Venkatesh, H. , Pandey, V., Kar, G., Mukherjee, J., Vyas, S., Gadgil, A.S., Patel, N.K.: Latent heat flux estimation in clear sky days over Indian agroecosystems using noontime satellite remote sensing data, Agric For Meteorol, 149(10), 1646 – 1665, https://doi.org/10.1016/j.agrformet.2009.05.006, 2009.

Mallick, K., Boegh, E., Trebs, I., Alfieri, J., Kustas, W., Prueger, J., Niyogi, D., Das, N., Drewry, D., Hoffmann, L. and Jarvis, A.: Reintroducing radiometric surface temperature into the Penman-Monteith formulation, Water Resour. Res., 51(8), 6214 – 6243, https://doi.org/10.1002/2014WR016106, 2015a.

Mallick, K., Jarvis, A., Boegh, E., Fisher, J., Drewry, D., Tu, K., Hook, S., Hulley, G., Ardö, J., Beringer, J., Arain, A. and Niyogi, D.: A Surface Temperature Initiated Closure (STIC) for surface energy balance fluxes, Remote Sens. Environ., 141, 243 – 261, https://doi.org/10.1016/j.rse.2013.10.022, 2014.

Mallick, K., Jarvis, A., Wohlfahrt, G., Kiely, G., Hirano, T., Miyata, A., Yamamoto, S., and Hoffmann, L.: Components of near-surface energy balance derived from satellite soundings – Part 1: Noontime net available energy, Biogeosci., 12, 433–451, https://doi.org/10.5194/bg-12-433-2015, 2015b.

Mallick, K., Toivonen, E., Trebs, I., Boegh, E., Cleverly, J., Eamus, D., Koivusalo, H., Drewry, D., Arndt, S., Griebel, A., Beringer, J. and Garcia, M.: Bridging thermal infrared sensing and physically-based evapotranspiration modeling: from theoretical implementation to validation across an aridity gradient in Australian ecosystems, Water Resour. Res., 54(5), 3409 – 3435, https://doi.org/10.1029/2017WR021357, 2018a.

Mallick, K., Trebs, I., Boegh, E., Giustarini, L., Schlerf, M., Drewry, D., Hoffmann, L., von Randow, C., Kruijt, B., Araùjo, A., Saleska, S., Ehleringer, J., Domingues, T., Ometto, J.,

983 Nobre, A., de Moraes, O., Hayek, M., Munger, J. and Wofsy, S.: Canopy-scale biophysical
984 controls of transpiration and evaporation in the Amazon Basin, Hydrol. Earth Syst. Sci., 20,
985 4237–4264, doi:10.5194/hess-20-4237-2016, 2016.
986 Mallick, K., Wandera, L., Bhattarai, N., Hostache, R., Kleniewska, M. and Chormanski, J.: A
987 Critical Evaluation on the Role of Aerodynamic and Canopy–Surface Conductance
988 Parameterization in SEB and SVAT Models for Simulating Evapotranspiration: A Case
989 Study in the Upper Biebrza National Park Wetland in Poland, Water, 10(12), 1753,
990 https://doi.org/10.3390/w10121753, 2018b.
991 Mallick, K., Baldocchi, D., Jarvis, A., Hu, T., Trebs, I., Sulis, M., et al.: Insights into the
992 aerodynamic versus radiometric surface temperature debate in thermal-based evaporation
993 modeling. Geophys. Res. Let., 49, e2021GL097568. https://doi.org/10.1029/2021GL097568,
994 2022.
995 Maltese, A., Bates, P., Capodici, F., Cannarozzo, M., Ciraolo, G. and La Loggia, G.: Critical
996 analysis of thermal inertia approaches for surface soil water content retrieval, Hydrol. Sci. J.,
997 58(5),1144-1161, https://doi.org/10.1080/02626667.2013.802322, 2013.
998 Martel, M., Glenn, A., Wilson, H. and Kröbel, R.: Simulation of actual evapotranspiration from
999 agricultural landscapes in the Canadian Prairies, J. Hydrol. Reg. Stud., 15, 105 – 118,
1000 https://doi.org/10.1016/j.ejrh.2017.11.010, 2018.
1001 Matheny, A., Bohrer, G., Stoy, P., Baker, I., Black, A., Desai, A., Dietze, M., Gough, C.,
1002 Ivanov, V., Jassal, R., Novick, K., Schäfer, K. and Verbeeck, H.: Characterizing the diurnal
1003 patterns of errors in the prediction of evapotranspiration by several land-surface models: An
1004 NACP analysis, J. Geophys. Res. Biogeosci., 119(7), 1458 – 1473,
1005 https://doi.org/10.1002/2014JG002623, 2014.
1006 Minasny, B.& Hartemink, A. E.: Predicting soil properties in the tropics. Earth-Science Rev.,1 –
1007 2, 52 – 62, https://doi.org/10.1016/j.earscirev.2011.01.005, 2011.
1008 Mihailovic, D. T., Kallos, G., Aresenic, I.D., Lalic, B., Rajkovic, B. and Papadopoulos, A.:
1009 Sensitivity of soil surface temperature in a Force-Restore Equation to heat fluxes and deep
1010 soil temperature. Intl. J. Climatol., 19, 1617-1632, 1999.
1011 Monteith, J &Unsworth, M.: Principles of Environmental Physics: Plants, Animals, and the
1012 Atmosphere, Fourth Edition, 1-401, 2013.

1013 Moran, M. S., Jackson, R. D., Raymond, L. H., Gay, L. W. and Slater, P. N.: Mapping surface
1014 energy balance components by combining landsat thematic mapper and ground-based
1015 meteorological data, Remote Sens. Environ., 30, 77 – 87, https://doi.org/10.1016/0034-
1016 4257(89)90049-7, 1989.
1017 Morisson, R., Angadi, S. S., Cooper, H. M., Evans, J. G., Rees, G., Sekhar, M., Taylor, C.,
1018 Tripathi, S. N. and Turner, A. G. : Energy and carbon dioxide fluxes, meteorology and soil
1019 physics observed at INCOMPASS land surface stations in India, 2016 to 2017, NERC
1020 Environmental Information Data Centre, doi:10.5285/78c64025-1f8d-431cbdeb-
1021 e69a5877d2ed, 2019b.
1022 Morisson, R., Angadi, S. S., Cooper, H. M., Evans, J., Rees, G., Sekhar, M., Taylor, C.,
1023 Tripathi, S. N. and Turner, A. G. : High temporal resolution meteorology and soil physics
1024 observations from INCOMPASS land surface stations in India, 2016 to 2018, NERC
1025 Environmental Information Data Centre, doi:10.5285/c5e72461-c61f-4800- 8bbf-
1026 95c85f74c416, 2019a.
1027 Murray, T. and Verhoef, A.: Moving towards a more mechanistic approach in the determination
1028 of soil heat flux from remote measurements, Agric. For. Meteorol., 147(1-2), 80 – 87,
1029 https://doi.org/10.1016/j.agrformet.2007.06.009, 2007.
1030 Norman, J., Anderson, M., Kustas, W., French, A., Mecikalski, J., Torn, R., Diak, G.,
1031 Schmugge, T. and Tanner, B.: Remote sensing of surface energy fluxes at 10^1-m pixel
1032 resolutions, Water Resour. Res. 39(8), https://doi.org/10.1029/2002WR001775, 2003.
1033 Purdy, A., Fisher, J., Goulden, M. and Famiglietti, J.: Ground heat flux: An analytical review of
1034 6 models evaluated at 88 sites and globally, J. Geophys. Res.: Biogeosci., 121(12), 3045 –
1035 3059,https://doi.org/10.1002/2016JG003591, 2016.
1036 Raja, P., Singh, M., Singh, N., and Sinha, N.K.: Photosynthesis and Biomass studies in
1037 Lasiurussindicus of Chandan Grassland in Thar Desert, XXIII International Grassland
1038 Conference, New Delhi, Volume: IGC 2015, 2015.
1039 Santanello, J. and Friedl, M.: Diurnal Covariation in Soil Heat Flux and Net Radiation, J. Appl.
1040 Meteorol., 42(6), 851 – 862, https://doi.org/10.1175/1520-
1041 0450(2003)042<0851:DCISHF>2.0.CO;2, 2003.
1042 Schmid, H.P.: Footprint modelling for vegetation atmosphere exchange studies: a review and
1043 perspective. Agric. For. Meteorol., 113, 159-183, 2002.

Sauer T.J. and Horton, R.: Soil Heat flux, Micrometeorology in Agricultural Systems, Agronomy Monograph no. 47, American Society of Agronomy, Crop Science Society of America, Soil Science Society of America, 677 S. Segoe Rd., Madison, WI 53711, USA, 2005.

Schaaf, C., Gao, F., Strahler, A., Lucht, W., Li, X., & Tsang, T. , trugnell, N. C., Zhang, X., Jin, Y., Muller, J., Lewis, P., Barnsley, M., Hobson, P., Disney, M., Roberts, G., Dunderdale, M., Doll, C., d'Entremont, R. P., Hu, B., Liang, S., Privette, J. L. and Roy, D. : First operational BRDF, albedo nadir reflectance products from MODIS, Remote Sens. Environ., 83(1-2), 135-148, doi:10.1016/s0034-4257(02)00091-3, 2002.

Schymanski, S. J., Breitenstein, D., and Or, D.: Technical note: An experimental set-up to measure latent and sensible heat fluxes from (artificial) plant leaves, Hydrol. Earth Syst. Sci., 21, 3377–3400, https://doi.org/10.5194/hess-21-3377-2017, 2017.

Singh, A.: Integrated Water Management: Water and Plant Growth,1–16, 2007.

Stoy, P., Mauder, M., Foken, T., Marcolla, B., Boegh, E., Ibrom, A., Arain, M., Arneth, A., Aurela, M., Bernhofer, C., Cescatti, A., Dellwik, E., Duce, P., Gianelle, D., van Gorsel, E., Kiely, G., Knohl, A., Margolis, H., McCaughey, H., Merbold, L., Montagnani, L., Papale, D., Reichstein, M., Saunders, M., Serrano-Ortiz, P., Sottocornola, M., Spano, D., Vaccari, F. and Varlagin, A.:A data-driven analysis of energy balance closure across FLUXNET research sites: The role of landscape scale heterogeneity, Agric. For. Meteorol., 171 – 172, 137 – 152, https://doi.org/10.1016/j.agrformet.2012.11.004, 2013.

Su, Z.: The Surface Energy Balance System (SEBS) for estimation of turbulent heat fluxes, Hydrol. Earth Syst. Sci., 6, 85–100, doi:10.5194/hess-6-85-2002, 2002.

Tian, L., Zhang, Y., & Zhu, J.: Decreased surface albedo driven by denser vegetation on the Tibetan Plateau, Environ. Res. Lett., 9(10), 104001, doi:10.1088/1748-9326/9/10/104001, 2014.

Trebs, I., Mallick, K., Bhattarai, N., Sulis, M., Cleverly, J., Woodgate, W., Silberstein, R., Najera, H.-N., Beringer, J., Meyer, W. S., Su, Z., and Boullet, G.: The role of aerodynamic resistance in thermal remote sensing-based evapotranspiration models, Remote Sens. Environ., 264, 112602, doi:10.1016/j.rse.2021.112602, 2021

Tsuang, B.: Ground Heat Flux Determination according to Land Skin Temperature Observations from i*n-situ* Stations and Satellites, J. Hydrometeorol., 6(4), 371 – 390, https://doi.org/10.1175/JHM425.1, 2005.

Turner, A., Bhat, G., Martin, G., Parker, D., Taylor, C., Mitra, A., Tripathi, S., Milton, S., Rajagopal, E., Evans, J., Morrison, R., Pattnaik, S., Sekhar, M., Bhattacharya, B., Madan, R., Govindankutty, M., Fletcher, J., Willetts, P., Menon, A. and Marsham, J.: Interaction of convective organization with monsoon precipitation, atmosphere, surface and sea: The 2016 INCOMPASS field campaign in India, Q. J. R. Meteorolog. Soc., 1–25, https://doi.org/10.1002/qj.3633, 2019.

Van Dijk, A.I.J.M., Gash, J.H., Gorsel, E.V., Blanken, P.D., Cescatti, A., Emmel, C., Gielen, B., Harman, I.N., Kiely,G., Merbold, L., Montagnani, L., Moors, E., Sottocornola, M., Varlagin, A., Williams, C.A., Wohlfahrt, G.: Rainfall interception and the coupled surface water and energy balance, Agric For Meteorol., 214 – 215,402 – 415, https://doi.org/10.1016/j.agrformet.2015.09.006, 2015.

Van Genuchten, M.: A Closed-form Equation for Predicting the Hydraulic Conductivity of Unsaturated Soils, Soil Sci. Soc. Am. J., 44(5),892, https://doi.org/10.2136/sssaj1980.03615995004400050002x, 1980.

Venturini, V., Islam, S. and Rodriguez, L.: Estimation of evaporative fraction and evapotranspiration from MODIS products using a complementary based model, Remote Sens. Environ., 112(1),132 – 141, doi:10.1016/j.rse.2007.04.014,2008.

Verhoef, A., Ottlé, C., Cappelaere, B., Murray, T., Saux-Picart, S., Zribi, M., Maignan, F., Boulain, N., Demarty, J. and Ramier, D.: Spatio-temporal surface soil heat flux estimates from satellite data; results for the AMMA experiment at the Fakara (Niger) supersite, Agric. For. Meteorol., 154-155, 55 – 66, doi:10.1016/j.agrformet.2011.08.003,2012.

Verhoef, A.: Remote estimation of thermal inertia and soil heat flux for bare soil, Agric. For. Meteorol., 123(3-4), 221 – 236, doi:10.1016/j.agrformet.2003.11.005,2004.

Vesala, T., Kljun, N., Rannik, U., Rinne, A. Sogachev, Markkanen, T., Sabelfeld, K., Foken, T. and Leclerc, M.Y.: Flux and concentration footprint modelling: State of the art. Environ. Polln., 152, 653-666, 2008.

Wan, Z.: New refinements and validation of the collection-6 MODIS land-surface temperature/emissivity product, Remote Sens. Environ., 140, 36 – 45, doi:10.1016/j.rse.2013.08.027, 2014.

Wang, S., Yang, Y., Luo, Y., and Rivera, A.: Spatial and seasonal variations in evapotranspiration over Canada's landmass, Hydrol. Earth Syst. Sci., 17, 3561–3575, doi:10.5194/hess-17-3561-2013, 2013.

Wilson, K., Goldstein, A., Falge, E., Aubinet, M., Baldocchi, D., Berbigier, P., Bernhofer, C., Ceulemans, R., Dolman, H., Field, C., Grelle, A., Ibrom, A., Law, B., Kowalski, A., Meyers, T., Moncrieff, J., Monson, R., Oechel, W., Tenhunen, J., Valentini, R. and Verma, S.: Energy balance closure at FLUXNET sites, Agric. For. Meteorol., 113(1-4), 223 – 243, doi:10.1016/S0168-1923(02)00109-0,2002.

Winter, J. and Eltahir, E.: The Sensitivity of Latent Heat Flux to Changes in the Radiative Forcing: A Framework for Comparing Models and Observations, J. Clim., 23(9),2345-2356, doi:10.1175/2009JCLI3158.1,2010.

Zerefos, C. S. & Bais, A. F.: Solar Ultraviolet Radiation: Modelling, Measurements and Effects, Springer Berlin Heidelberg, 2013.

Appendix A

Table A1: A list of symbols, their descriptions and units used in the present study

Attributes	Symbol	Description
Temperature	T_A	Air temperature (^{o}C)
	T_{Max}	Maximum air temperature (^{o}C)
	T_{Min}	Minimum air temperature (^{o}C)
	T_D	Air dew-point temperature (^{o}C)
	T_{STA}	point-scale soil temperature amplitude
	ΔTs	noon-night LST difference (^{o}C)
	T_{ST}	Soil temperature (^{o}C)

	T_S	Land surface temperature (LST) (^{o} C)
Humidity, vapor pressures	R_H	Relative humidity (%)
	e_A	Atmospheric vapor pressure at the level of T_A measurement (hPa)
	e_A^*	Saturation vapor pressure at the level of T_A measurement (hPa)
	e_S^*	Saturation vapor pressure at surface (hPa)
	D_A	Atmospheric vapor pressure deficit at the level of T_A measurement (hPa)
Radiation	R_G	Downwelling shortwave radiation (or global radiation) (W m^{-2})
	R_R	Upwelling or reflected shortwave radiation (W m^{-2})
	$R_{L\downarrow}$	Downwelling longwave radiation (W m^{-2})
	$R_{L\uparrow}$	Upwelling longwave radiation (W m^{-2})
	τ_{sw}	Atmospheric transmissivity for shortwave radiation (unitless)
	α_R	Broadband shortwave surface albedo (unitless)
SEB components	LE_i	Latent heat flux (W m^{-2}); subscript 'i' signifies 'instantaneous'
	H_i	Sensible heat flux (W m^{-2}); subscript 'i' signifies 'instantaneous'
	G_i	Ground heat flux (W m^{-2}); subscript 'i' signifies 'instantaneous'
	R_{Ni}	Net radiation (W m^{-2}); subscript 'i' signifies 'instantaneous'
	ϕ	Net available energy (W m^{-2}); i.e., $R_N - G$
	A	Ecosystem-scale surface soil temperature amplitude(^{o}C)
	T_{Sd}	Daytime T_S (^{o} C)
	T_{Sn}	Nighttime T_S (^{o} C)
	ω	Angular frequency (rad s^{-1})
	ϕ'_n	Phase shift of the n^{th} soil surface temperature harmonic (rad)
	Δ	Shape parameter (unitless)
	S_r	Relative soil moisture saturation (m^3 m^{-3})

MV2007 model	f_s	Sand fraction (unitless)
	θ_{fc}	Soil water content at field capacity ($m^3\ m^{-3}$)
	θ_{wp}	Soil water content at permanent wilting point ($m^3\ m^{-3}$)
	θ_*	Soil porosity ($cm^3\ cm^{-3}$)
	J_S	Summation of harmonic terms of soil surface temperature (K)
	Υ'	Soil textural parameter (unitless)
	Γ	Soil thermal inertia ($J\ K^{-1}\ m^{-2}\ s^{-0.5}$)
	τ_0	Thermal inertia of air-dry soil ($J\ K^{-1}\ m^{-2}\ s^{-0.5}$)
	τ_*	Thermal inertia of saturated soil ($J\ K^{-1}\ m^{-2}\ s^{-0.5}$)
	t’	Time of satellite overpass (seconds)
	Δt	Time offset between the canopy composite temperature and the below-canopy soil surface temperature (seconds)
	κ	Total number of harmonics used (unitless)
	f_c	Vegetation fraction (unitless)
	θ	Volumetric soil moisture ($cm\ cm^{-3}$)
Clear-sky R_{Ni} model	R_{ns}	Net shortwave radiation ($W\ m^{-2}$)
	R_{nl}	Net long wave radiation ($W\ m^{-2}$)
	G_{sc}	Solar constant (1367 $W\ m^{-2}$)
	β_e	Sun elevation angle (^{0}).
	ε_s	Infrared surface emissivity (unitless)
	ε_a	Atmospheric emissivity (unitless)
	E	Eccentricity correction factor due to variation in Sun-Earth distance (unitless)
	M	Aggregated moisture availability (0-1)

STIC-TI model	g_A	Aerodynamic conductance (m s^{-1})
	g_S	Canopy-surface conductance (m s^{-1})
	T_0	Aerodynamic temperature (or source/sink height temperature) (^oC)
	T_{0D}	Dewpoint temperature at the source/sink height (^oC)
	Λ	Evaporative fraction (unit less)
	e_0	Vapor pressure at the source/sink height (hPa)
	e_0^*	Saturation vapor pressure at the source/sink height (hPa)
	D_0	Vapor pressure deficit at source/sink height (hPa)
	s_1	Psychrometric slope of vapor pressure and temperature between (T_{0D} -T_D) versus (e_0 -e_A) (h Pa K^{-1})
	s_2	Psychrometric slope of vapor pressure and temperature between (T_S-T_D) versus (e_s^*-e_A) (h Pa K^{-1})
	s_3	Psychrometric slope of vapor pressure and temperature between (T_{0D} -T_D) versus (e_s^*-e_A).
	κ	Ratio between (e_0^* - e_A) and (e_s^* - e_A) (unitless)
	s	Slope of saturation vapor pressure vs. temperature curve (h Pa K^{-1})
	α	Priestley-Taylor coefficient (unitless)
Ancillary meteorological variables	U	Wind speed at 8 m height (m s^{-1})
	u^*	Friction velocity (m s^{-1})
Constants	P	Precipitation (mm d^{-1})
	γ	Psychrometric constant (h Pa k^{-1})
	c_p	Specific heat capacity of air at constant pressure (MJ kg^{-1} K^{-1})
	ρ	Density of air (Kg m^{-3})

	σ	Stefan–Boltzmann constant (5.67 x 10 $^{-8}$ $Wm^{-2}K^{-4}$)

1120

1121

1122 **Table A2:** Summary of instruments used, height or depth and period of measurements, measured
1123 variables at nine EC flux tower sites

Type of primary instruments used for in situ data recording at flux tower sites	**Measurement Height/ Depth (m) at different sites**	**Measured variables**
Net radiometer	• 3m (IND-Naw, IND-Jai, IND-Sam) • 15m (AU-Ade) • 12.2m (AU-ASM) • 23m (AU-How)2m (US-Ton, US-Var)	Four radiation flux components: shortwave incoming (R_G**)** and outgoing (R_R**)**; longwave incoming ($R_L\downarrow$**)** and outgoing ($R_L\uparrow$**)**
EC assembly with IRGA (Infrared Gas Analyzer), three-dimensional sonic anemometer, TC probe	• 8m (IND-Naw; IND-Jai; IND-Sam) • 4.5m (IND-Dha) • 15m (AU-Ade) • 11.6m(AU-ASM) • 23m (AU-How) • 2m (US-Ton, US-Var)	High response wind vectors (*u*, *v* and *w)*, sonic temperature, and CO_2- water vapor mass at 10/20 Hz frequency
Humidity and temperature probe	• 8m (IND-Naw, IND-Jai, IND-Sam) • 4.5m (IND-Dha) • 15m (AU-Ade), 11.6m (AU-ASM) • 23m (AU-How), 70m (AU-How) • 2m (US-Ton, US-Var)	T_A and R_H
Soil temperature probe	• -0.1m (IND-Dha) • -0.15m (AU-Ade) • (-0.02, -0.06m) (AU- ASM) • -0.08m (AU- How) • -0.02m, -.0.04m, -0.08m, and -0.16m (US-Ton, US-Var)	T_{ST}
Soil heat flux plates	• Ground, 0.1 m (IND-Dha) • Ground, -0.15 m (AU-Ade) • Ground, -0.08 m (AU-ASM) • Ground, -0.15 m (AU-How) • -0.01m (US-Ton, US-Var)	Soil heat flux (G)

Appendix B

B1: Clear-sky instantaneous net radiation (R_{Ni}) model

Net radiation (R_N) is defined as the difference between the incoming and outgoing radiation fluxes, which includes both longwave and shortwave radiation at the surface of earth.

Terrestrial R_N has four components: downwelling and upwelling shortwave radiation (R_G and R_R), downwelling and upwelling longwave radiation ($R_{L\downarrow}$ and $R_{L\uparrow}$), respectively.

$$R_N = (R_G - R_R) + (R_{L\downarrow} - R_{L\uparrow}) \quad \text{(B1)}$$

Out of these four terms mentioned in eq.(B1), R_G and $R_{L\downarrow}$ are dependent on various factors such as geographic location, season, cloudiness, aerosol loading, atmospheric water vapor content and less on surface properties. On the other hand, the upwelling radiations in eq. (B1) strongly depends on the surface properties such as surface reflectance and emittance, land surface temperature, and soil water content (Zerefos and Bais, 2013).

Instantaneous net radiation (R_{Ni}) can be derived using eq. B2 as follows (Mallick et al., 2007):

$$R_{Ni} = R_{ns} - R_{nl} \quad \text{(B2)}$$

$$R_{ns} = (1 - \alpha_R)\, R_G \quad \text{(B3)}$$

$$R_{nl} = R_{L\downarrow} - R_{L\uparrow} \quad \text{(B4)}$$

Where, R_{ns} is net shortwave radiation (W m^{-2}), R_{nl} is net longwave radiation (W m^{-2}).and $\alpha_R$is the broadband surface albedo shortwave spectrum.

A WMO (World Meteorological Organization) shortwave radiation model (Cano et al.,1986) calibrated over Indian conditions (Mallick et al., 2007, 2009) was used to compute R_G using the following equation:

$$R_G = \tau_{sw} G_{sc} E\, (\sin\beta_e)^{1.15} \quad \text{(B5)}$$

Where,τ_{sw} is the is the global clear sky transmissivity for the shortwave radiation (0.7), G_{sc} is the solar constant (1367 Wm^{-2}), ε is the eccentricity correction factor due to variation in Sun-Earth distance and β_e is the sun elevation in degrees.

$R_L\downarrow$at any instance was calculated as follows:

$$R_{L\downarrow} = \varepsilon_a \, \sigma \, (273.14 + T_A)^4 \quad \text{(B6)}$$

Where, σ is the Stefan–Boltzmann constant (5.67 $x10^{-8}$ $Wm^{-2}K^{-4}$); T_A is the air temperature (^{0}C); ε_a is the atmospheric emissivity.

Atmospheric emissivity (ε_a) was computed using the following equation (Bastiaanssen et al.,1998):

$$\varepsilon_a = 0.85 - \ln\tau_{sw}{}^{0.09} \quad \text{(B7)}$$

$R_L\uparrow$at any particular instance was calculated as follows:

$$R_{L\uparrow} = \varepsilon_s \, \sigma(273.14 + T_s)^4 \quad \text{(B8)}$$

Where, $\varepsilon_s$is the surface emissivity in thermal infrared (8 – 14 μm) spectrum and T_S is the land surface temperature (^{0}C).

B2: Evaluation of STIC-TI R_{Ni}

Comparison of the clear-sky R_{Ni} estimates with respect to *in situ* measurements revealed RMSE in R_{Ni} to the order of 27 – 72 W m^{-2}, MAPD 8 –24%, BIAS (-67) – 50 W m^{-2}, and R^2 varying from 0.62– 0.90 across all the sites (Fig. B2, Table B2). Among the nine sites, a consistent underestimation of R_{Ni} was noted in IND-Dha, US-Ton, and US-Var (with BIAS of -23 W m^{-2}, -61 W m^{-2} and -67 W m^{-2}), whereas substantial overestimation of R_{Ni} was found in IND-Sam, IND-Naw, and AU-ASM with a BIAS of 50 W m^{-2}, 37 W m^{-2} and 43 W m^{-2}, respectively (Table B2).

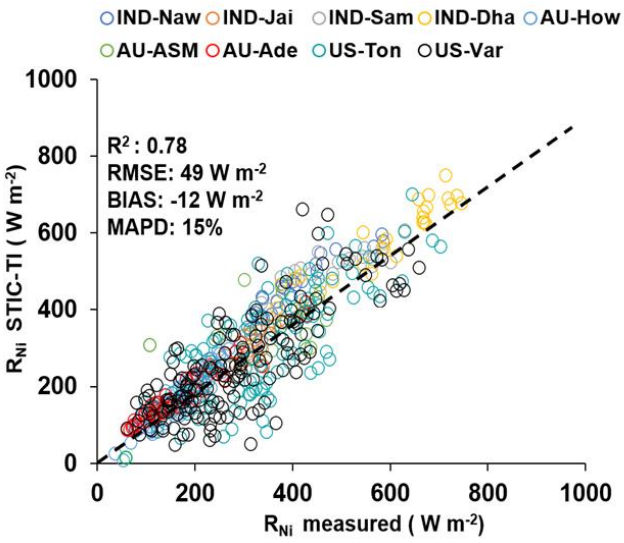

Figure B2: Validation of STIC-TI derived R_{Ni} estimates with respect to *in situ* measurements in different ecosystems. The regression equation between modeled versus in-situ R_{Ni} is, R_{Ni} (STIC-TI) = 0.78R_{Ni} (tower) +58.92.

Table B2: Performance evaluation statistics of clear-sky R_{Ni} estimates in nine different agroecosystems

Sites	**Error statistics of clear-sky R_{Ni} model estimates**			
	R^2	**BIAS ($W\ m^{-2}$)**	**RMSE ($W\ m^{-2}$)**	**MAPD (%)**
IND-Jai	0.81	-9	32	8
IND-Naw	0.81	37	56	12
IND-Dha	0.81	-23	42	9
IND-Sam	0.64	50	67	15
US-Ton	0.68	-61	69	21
US-Var	0.62	-67	72	24
Au-How	0.87	7	27	15
AU-ASM	0.88	43	50	14
AU-Ade	0.90	11	27	16

Appendix C

C1: Estimating SEB fluxes using STIC1.2 analytical model and thermal remote sensing data

STIC1.2 (Mallick et al., 2014, 2015a,b, 2016, 2018a) is a one-dimensional physically based SEB model and is based on the integration of satellite LST observations into the Penman–Monteith Energy Balance (PMEB) equation (Monteith, 1965). In STIC1.2, the vegetation–substrate complex is considered as a single slab. Therefore, the aerodynamic conductances from individual air-canopy and canopy-substrate components is regarded as an 'effective' aerodynamic conductance (g_A), and surface conductances from individual canopy (stomatal) and substrate complexes is regarded as an 'effective' canopy-surface conductance (g_S) which simultaneously regulate the exchanges of sensible and latent heat fluxes (H and LE) between surface and atmosphere. One of the fundamental assumptions in STIC1.2 is the first order dependence of these two critical conductances on M through T_S. Such an assumption enabled an integration of satellite LST in the PMEB model (Mallick et al., 2016). The common expression for LE and H according to the PMEB equation is as follows:

$$LE = \frac{s\phi + \rho c_P g_A D_A}{s + \gamma\left(1 + \frac{g_A}{g_S}\right)} \tag{C6}$$

$$H = \frac{\gamma\phi\left(1 + \frac{g_A}{g_S}\right) - \rho c_P g_A D_A}{s + \gamma\left(1 + \frac{g_A}{g_S}\right)} \tag{C7}$$

In the above equations, the two biophysical conductances (g_A and g_S) are unknown and the STIC1.2 methodology is based on finding analytical solutions for the two unknown conductances to directly estimate LE (Mallick et al., 2016, 2018a). The need for such analytical estimation of these conductances is motivated by the fact that g_A and g_S can neither be measured at the canopy nor at larger spatial scales, and there is no universally agreed appropriate model of g_A and g_S that currently exists (Matheny et al., 2014; van Dijk et al., 2015). By integrating T_S with standard SEB theory and vegetation biophysical principles, STIC1.2 formulates multiple

state equations in order to eliminate the need to use the empirical parameterizations of the g_A and g_S and also to bypass the scaling uncertainties of the leaf-scale conductance functions to represent the canopy-scale attributes. The state equations for the conductances are expressed as a function of those variables that are mostly available as remote sensing observations and weather forecasting models. In the state equations, a direct connection to T_S is established by estimating M as a function of T_S. The information of M is subsequently used in the state equations of conductances, aerodynamic variables (aerodynamic temperature, aerodynamic vapor pressure), and evaporative fraction, which is eventually propagated into their analytical solutions. M is a unitless quantity, which describes the relative wetness (or dryness) of a surface and also controls the transition from potential to actual evaporation; which implies $M \rightarrow 1$ under saturated surface conditions and $M \rightarrow 0$ under extremely dry conditions. Therefore, M is critical for providing a constraint against which the conductances are estimated. Since T_S is extremely sensitive to the surface moisture variations, it is extensively used for estimating M in a physical retrieval scheme (detail in Appendix A3 of Bhattarai et al., 2018; Mallick et al., 2016, 2018a). It is hypothesized that linking M with the conductances will simultaneously integrate the information of T_S into the PMEB model. To illustrate, we express the state equations by symbols, $sv_1 = f\{c_1, c_2, c_3, v_1, v_2, v_3, v_4, sv_3, sv_5\}$; $sv_2 = f\{v_4, sv_1, sv_5, sv_6\}$; $sv_3 = f\{c_3, v_3, v_4, sv_4, sv_5\}$; $sv_4 = f\{c_3, v_3, sv_1, sv_2, sv_7, sv_8\}$. Here, f, sv, v, and c denote the function, state variables, input variables (5 input variables; radiative and meteorological), and constants (3 constants), respectively. Here sv_1 to sv_4 are g_A, g_S, aerodynamic temperature (T_0), evaporative fraction (Λ), and sv_8 is M. Given the estimates of M, net radiative energy ($R_{N\,i} - G_i$), T_A, R_H, the four state equations are solved simultaneously to derive analytical solutions for the four state variables and to produce a surface energy balance "closure" that is independent of empirical parameterizations for g_A, g_S, T_0, and Λ. However, the analytical solutions to the four state equations contain three accompanying unknown state variables (effective vapor pressures at source/sink height, and Priestley-Taylor variable), and as a result there are four equations with seven unknowns. Consequently, an iterative solution was found to determine the three additional unknown variables as detailed in this section above and also described in Mallick et al. (2016, 2018a) and Bhattarai et al. (2018). The state equations of STIC are given below.

$$g_A = \frac{\phi}{\rho c_P \left[(T_0 - T_A) + \left(\frac{e_0 - e_A}{\gamma} \right) \right]} \quad \text{(C1)}$$

$$g_S = g_A \frac{(e_0 - e_A)}{(e_0^* - e_0)} \quad \text{(C2)}$$

$$T_0 = T_A + \left(\frac{e_0 - e_A}{\gamma} \right) \left(\frac{1 - \Lambda}{\Lambda} \right) \quad \text{(C3)}$$

$$\Lambda = \frac{2\alpha s}{2s + 2\gamma + \gamma \frac{g_A}{g_S}(1 + M)} \quad \text{(C4)}$$

Detailed derivations of these four state equations are given in Mallick et al. (2016). Given the values of M, R_N, G, T_A, and R_H or e_A, the four state equations can be solved simultaneously to derive analytical solutions for the four unobserved variables and to simultaneously produce a 'closure' of the PMEB model that is independent of empirical parameterizations for both g_A and g_S. However, the analytical solutions to the four state equations contain three accompanying unknowns; e_0 (vapor pressure at the source/sink height), e_0^* (saturation vapor pressure at the source/sink height), and Priestley-Taylor coefficient (α), and as a result there are four equations with seven unknowns. Consequently, an iterative solution was needed to determine the three unknown variables (as described in Appendix A2 in Mallick et al. 2016). Once the analytical solutions of g_A and g_S are obtained, both variables are returned into eq. (13) to directly estimate LE.

In STIC-TI, an initial value of α was assigned as 1.26; initial estimates of e_0^* were obtained from T_S through temperature-saturation vapour pressure relationship, and initial estimates of e_0 were obtained from M as, $e_0 = e_A + M(e_0^* - e_A)$. Initial T_{0D} and M were estimated according to Venturini et al. (2008) as described in section 3.2, and initial estimation of G was performed from initial M using the equation sets eq. (2) – eq. (11). With the initial estimates of these variables; first estimate of the conductances, T_0, Λ, H, and LE were obtained. The process was then iterated by updating e_0^*, D_0, e_0, T_{0D}, M, and α (using eq. A9, A10, A11, A17, A16 and A15 in Mallick et al., 2016), with the first estimates of g_S, g_A, T_0, and LE, and re-computing G, ϕ, g_S, g_A, T_0, Λ, H, and LE in the subsequent iterations with the previous estimates of e_0^*, e_0, T_{0D}, M,

and α until the convergence of LE was achieved. Stable values of G, conductances, LE, H, T_0, e_0^*, e_0, T_{0D}, M, and α were obtained within ~25 iterations. The inputs needed for computation of LE_i (eq.C6) are air temperature (T_A), land surface temperature (T_S), relative humidity (R_H), net radiation (R_{Ni}) and soil heat flux (G_i).

Appendix D

The temporal variation of estimated A and T_{STA} is shown in Fig. D1. The annual variations of T_{STA} in different ecosystem was found to be within the ranges of 1 - 4°C.

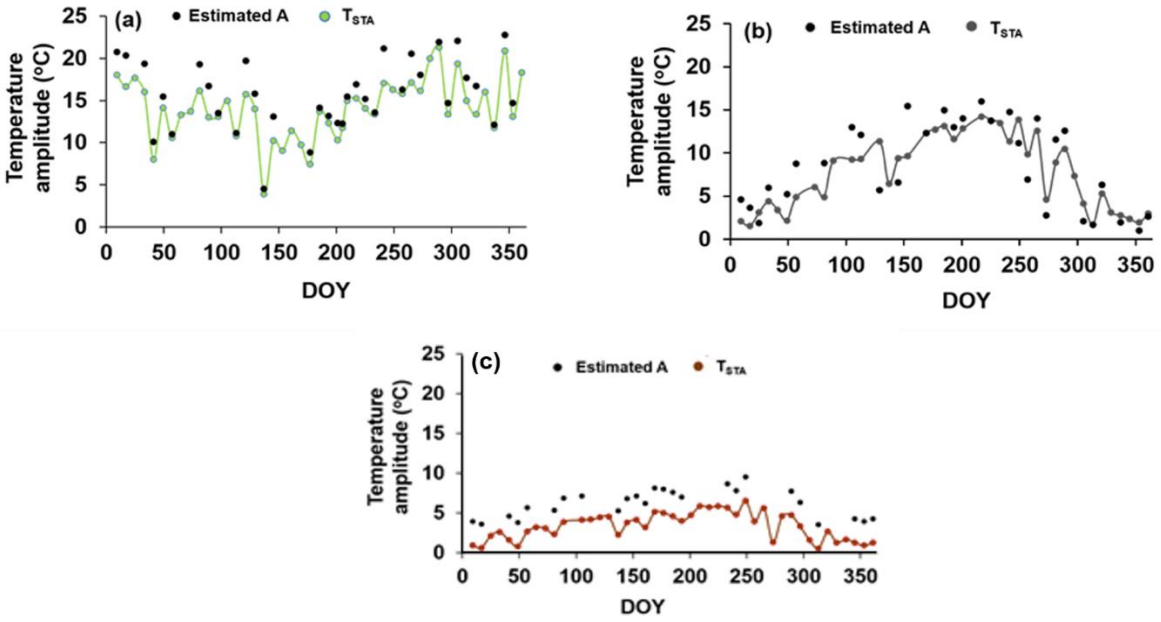

Figure D1: Temporal variation of A and T_{STA} in (a) AU-ASM (2013), (b) US-Ton (2014), (c) US- Var (2014).

Appendix E

Table E1: Soil textural properties and their values used in the present study (Murray and Verhoef, 2007; Minasny et al., 2011; Anderson et al., 2007)

Soil texture	**Water retention Shape parameter (δ)**	**Field capacity (vol/vol) (%) θ_{fc}**	**Wilting point (vol/vol) (%) θ_{wp}**	**Sand fraction (f_s)**	**Saturated soil moisture (vol/vol) (%) θ_***
Sand	2.77	10	5	0.92	43
Loamy Sand	2.39	12	5	0.82	41
Sandy loam	2.27	18	8	0.58	41
Loam	2.20	28	14	0.43	43
Silty loam	2.22	31	11	0.17	45
Sandy clay loam	2.17	27	17	0.58	39
Clay loam	2.14	36	22	0.40	41
Silty clay loam	2.14	38	22	0.10	43
Sandy clay	2.11	36	25	0.52	38
Silty clay	2.12	41	27	0.06	46
Clay	2.10	42	30	0.22	38

Appendix F

Day view angle effect on deviations of STIC-TI heat flux estimates from measurements is shown in Figure F.

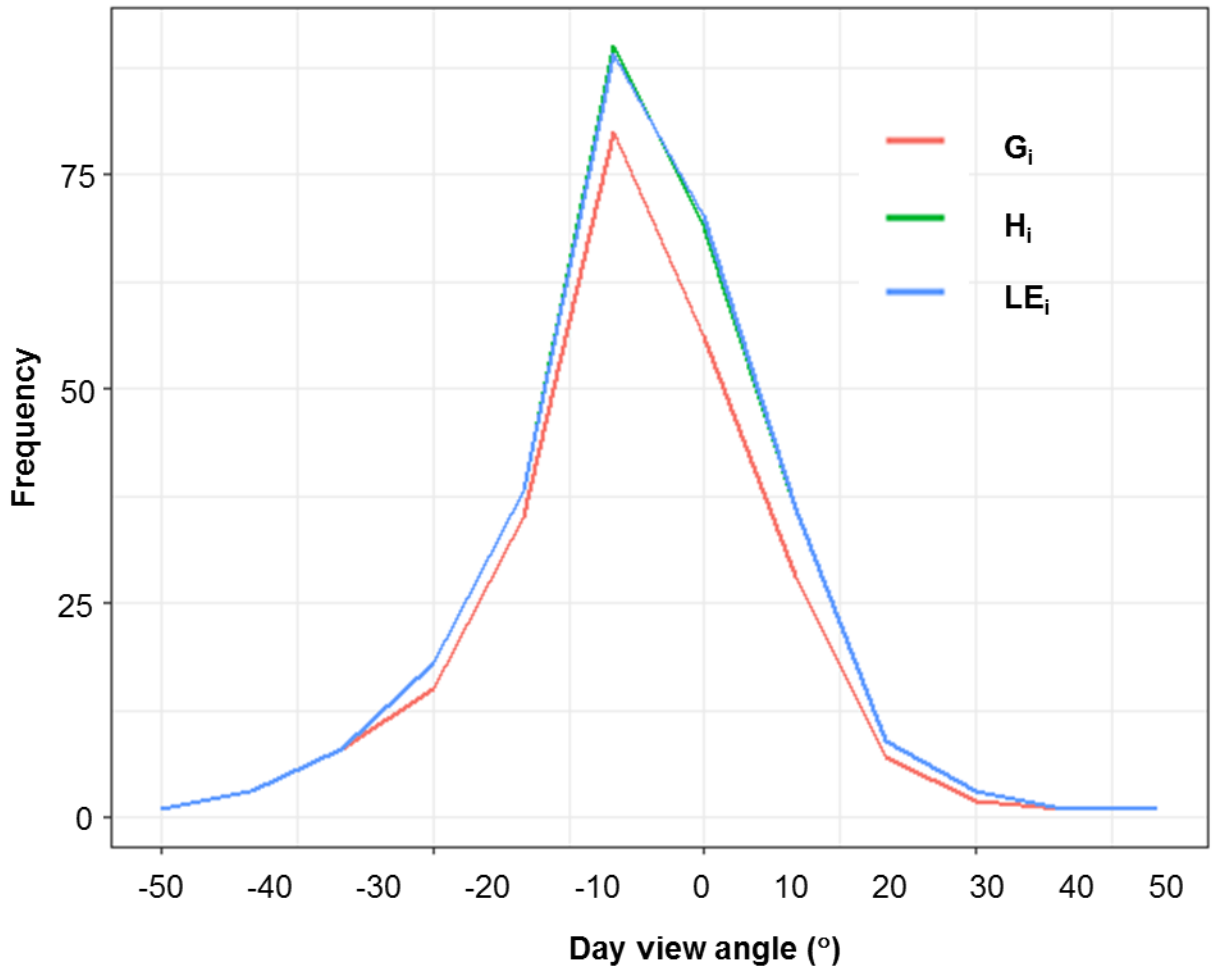

Figure F: Number of occurrences of deviations of STIC-TI heat flux estimates (G_i, H_i, LE_i) from measurements in each 10° bin within ±50° day view angle of MODIS Aqua